GROWTH AND MODELLING OF InGaP NANOWIRES BY MBE

GROWTH AND MODELLING OF InGaP NANOWIRES BY MBE

By

Ahmed Fakhr, M.A.Sc

A Thesis

Submitted to the School of Graduate Studies

in Partial Fulfilment of the Requirements

for the Degree

Doctor of Philosophy

McMaster University

DOCTOR OF PHILOSOPHY (2013) McMaster University

(Department of Electrical and Computer Engineering)

TITEL:	GROWTH AND MODELLING OF InGaP NANOWIRES BY MBE
AUTHOR:	Ahmed Fakhr (McMaster University)
SUPERVISOR:	Dr. Y. M. Haddara Dr. R. R. LaPierre
NUMBER OF PAGES:	xi, 100

Abstract

The growth of ternary InGaP nanowires (NWs) is explored. Free-standing NWs are grown with the Au nanoparticle-assisted method using a gas source molecular beam epitaxy (GS-MBE) system. The grown samples were characterized using scanning electron microscopy (SEM), transmission electron microscopy (TEM) and energy dispersive x-ray spectroscopy (EDX). These characterization techniques were employed to examine the composition of the InGaP NWs, the morphology and the crystal structure. With varying the growth conditions, such as temperature, growth rate and V/III flux, a dependence of the NWs' composition, morphology and crystal structure were observed. In addition, the characteristics of the NWs showed great dependence on the diameter of the Au seed particle responsible for the NW growth.

A physical-based growth model is developed to understand the NW growth results. The model deals with each of the group-III growth species differently and splits the group-V into two components, with each component associated with one of the group-III species. The model is able to match composition and morphology results obtained from the experimental data.

Furthermore, a nucleation-based model is employed and integrated with the growth model to predict the crystal structure of the NWs. Based on this model, the operating regions for all out samples were illustrated. In addition, the dependence of the crystal structure of the NWs on the Au seed diameter, in our samples, was attributed to the change in the surface energies of the formed nucleus as the Au seed diameter change.

Acknowledgment

The journey through the PhD studies is one that starts from the unknown, with the unknown leading the way, hoping to see "the lights at the end of the tunnel"(*R. LaPierre*). Along my journey through the unknown, I have met many people to whom I owe great appreciation and gratitude.

I would like to thank Dr. Haddara for giving me the chance and opportunity to start my PhD studies. He always believed in me when I was the one with most doubt about myself.

Along the dark times, I had Dr. LaPierre to hold the torch and direct me to the right path. His insights, determination and work ethics always managed to impress and guide me. I also greatly appreciate his support and help when I was in desperate need for one.

I am grateful to the staff of the ECE department, that created a friendly working environment. Thanks to Cosmin, Terry Greenlay, Helen Jachna and Alexa Huang, Danielle Marcellin and Steve Spencer. I am most grateful to Cheryl Gies, the mother of all grad students, for taking care of me and all the others. She manages a family of more than 200 graduate students and always have time to give more and listen with compassion.

Thanks for the members of the CEDT team for their efforts, Doris, Zhilin, Dr. Brad Robinson and Dr. Sharham Tavakoli. I would also like to thank the members of the BIMR Dr. Steve Koprich, Dr. Carmen Andrei, Andy Duft and Julia Huang. I have spent long hours in the dark rooms of the electron microscopy and I appreciate the effort Fred Pearson did to accommodate me when I needed to use urgently utilize the TEM microscope. I also appreciate his effort in making the microscopy sessions pleasant and informative with lot of helpful suggestions.

Fellow group members of the Haddara and LaPierre group has been great colleagues and friends. I appreciate the friendship of the Haddara group members: Ali, Has Su, Munir, Rabie and Hasanuzzaman, as well as the LaPierre group members: Martin, Parsian, Chris, Subir and Nuzhat.

For me to come to Canada and feel it is my home, I needed the support of many people. Thanks to my Aunt that helped to put my first steps in Canada. I cherish the group of friends that I made here that became like a family to me: Hossam, Tarek, Peter, Nermo, Fouly, Lamiaa, Shahin, Ghada, Hassan, Noha, Rami, Marwa and Julia. I love you all.

The love and support of my parents always gave me comfort during hard times. Your trust in me always gave me the confidence that I sometimes lacked. I am so grateful for you. Thanks to my brother Omar and my sister-in-law Steffi, I wish you all the happiness together.

My work would not have been tolerable without having my loving and patient wife, Noha, by my side. We started our journey together and it has been a great one so far. You tolerated me when thing were really tough on me and always gave me your wise opinions. I am indeed lucky to have you in my life and have been greatly blessed by my two beautiful kids Nora and Maged. Spending time with them was always a great way to cheer me up.

to my loving wife, Noha

Table of Contents

List of Figures

List of Tables

Chapter 1

Background

1.1 Au -Assisted Nanowires

The 20th century have witnessed the start and the boom of the planar semiconductor industry. Planar device fabrication introduced advances in electronics, computing and communications that we live in nowadays. Due to many road blocks [1] facing its further advancements, new devices are being explored to take over the technological advancements through the 21st century and among these devices are Nanowires. Nanowires are filament like structures with high length to diameter ratio, having their diameters ranging from few nanometers to few hundred nanometers and length that can exceed few micrometers. This unique shape of the nanowires promotes them to have superior electrical [2]-[4] and optical [5]-[6] performances when used in device fabrication. In addition, their nature of having a large lateral surface area compared to their volume makes their performance highly affected by their surface states, which makes them excellent candidates when used as sensors [7]-[8].

Planar epitaxial growth extends on the surface and advances upwards as the each monolayer is filled with atoms. Meanwhile, the main approach to synthesize nanowires is to force anisotropic growth that promotes crystal growth that favors one direction only. Several techniques have been employed to synthesize nanowires, as shown in Figure 1.1. These techniques can be template-directed, where the anisotropic growth takes place in a physically confined area that promotes growth in one direction only. An example of this

Figure 1.1 Representation of 1D nanostructure assembly methods. (a) Template-assisted pore-filling method. (b) V-groove template method (c) Particle-assisted growth (d) Particle-free self-assembly (Adopted from [9]).

approach is pore-filling [10] and the v-growth template growth [11], shown in Figure 1.1 (a) and (b), respectively. Free-standing nanowires represent another type of these devices that does not require physically confined growth. Among these techniques are the mask-mediated selective-area growth [12], and particle-assisted nanowire growth [13], as shown in (c) and (d), respectively.

The work in this thesis focuses on the particle-assisted nanowire growth as the way of nanowire assembly, with utilizing Au as the assisting particles. Known for its noble element attributes that it does not oxidize, Au also has the advantage of creating eutectic mixes with other elements with very low melting points [14].

The synthesized nanowires devices have great advantages over the planar epitaxial counterparts, such as the ability to grow upward on any <1 1 1> plan surface [16], without the need to lattice match the nanowire with underlying substrate. In addition, when hetero-interfaces are created, the induced strain due to the mismatch of the new layers is relaxed on the sidewall lateral surfaces [18], which allows for any combination of hetero-structures to be synthesized. Finally, having a free-standing nanowire puts it in the class of 3D devices, where devices can be fabricated along the nanowire axially or radially, as show in Figure 1.2 (a) and (b), respectively.

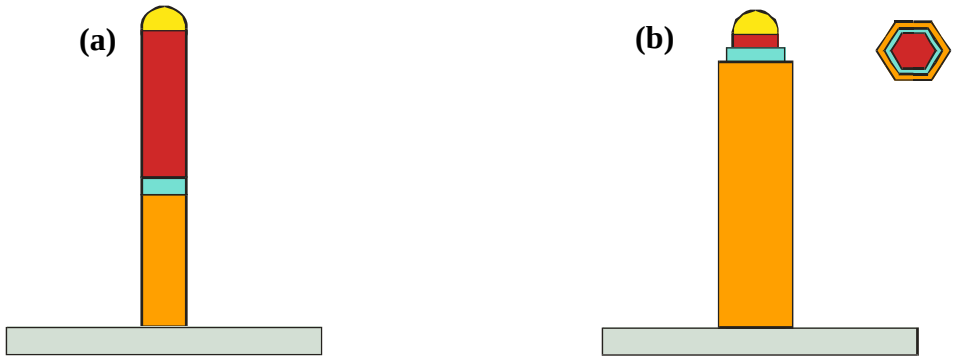

Figure 1.2 Metal-assisted grown nanowires with hetero-structures built (a) axially in the growth direction of the nanowire, and (b) radially as core/shell structures .

1.2 Driving Force for Nanowire Growth

The growth on the Au-assisted assembly requires the presence of Au on the surface prior to growth. The Au particles can be uniformly placed on the surface by using electron-beam lithography [19]-[20], nano-imprinting [21]-[22], porous-alumina masked Au deposition [23]-[25], and block-copolymer assisted nanolithography [26]-[27]. However, these techniques require more processing steps that increase the cost of the fabrication and low yields, along with contamination of the surface [28].

Random placement of the Au seed particle is an alternative that provides ease in fabrication, lower cost and higher yield. Due the randomness of the NW distribution, the morphologies of the obtained yields from these techniques has the disadvantage of having

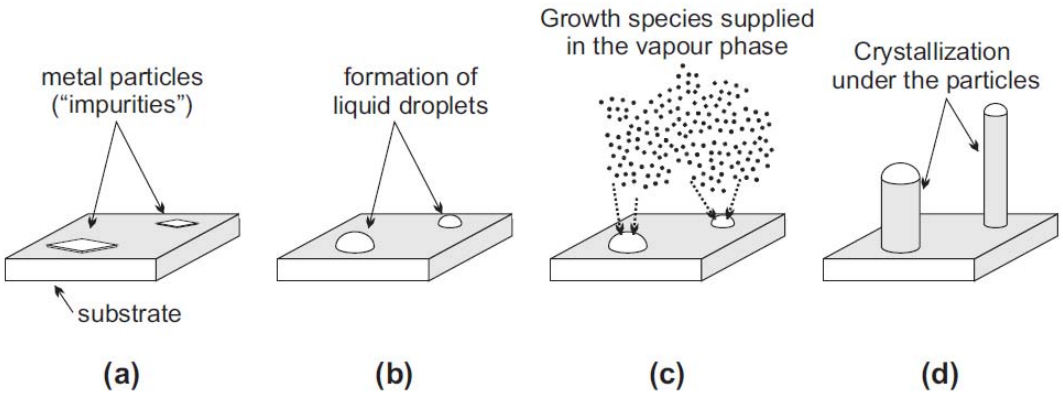

Figure 1.3: Illustration of the VLS mechanism. (a) "Impurities" (metallic particles) are initially present on a substrate surface. (b) The system is heated above the eutectic temperature to form the liquid alloy droplets. (c) Atoms directly supplied from the vapour phase get preferentially deposited on the liquid droplets. (d) Supersaturation of the liquid causes precipitation at the liquid-solid interface, and crystal growth follows (Adopted from [15]).

a high margins in error. These techniques include colloidal nanoparticle deposition through drop-casting, spray/spin coating on the substrate [29]-[31], covalent self-assembly of colloidal nanoparticles [32]-[35] and formation of nanoparticles based on the thermal dissociation of thin films [36]-[38]. The dissociation of thin films is the method used throughout the thesis. In this method, a thin layer of Au (1 nm) is deposited on the surface, as shown in Figure 1.3 (a). As the sample is annealed, the thin Au film dissociates and forms droplets on the surface. The droplets have the ability to diffuse on the surface and undergo Ostwald ripening, leaving a nonuniform distribution of Au nano-particles on the surface, with wide distribution of diameters, as shown in Figure 1.3 (b).

When growth is introduced, the growth species in the vapor phase, reach the Au particles on the surface and mixes with them, forming an eutectic alloy in the liquid

phase, as shown in Figure 1.3 (c). As the growth species continue to approach the eutectic alloy, the eutectic alloy becomes supersaturated with the growth species and any addition of excess growth species to the alloy, results in material precipitating from the alloy droplet at the underlying interface to create a layer of a crystalline solid. Introducing more of the growth species sustains this process and growth of a crystalline nanowire takes place underneath the alloy droplet. This process of transforming the growth species from the vapor phase (V), into the liquid eutectic alloy (L) and finally, precipitating it as a crystalline solid (S), is known as the vapor-liquid-solid mechanism (VLS).

The VLS process can occur at temperatures that are below the melting point of the eutectic alloy. In this case the alloy stays in the solid state and the growth mechanism is then called, the vapor-solid-solid (VSS) mechanism [39]-[40]. In conclusion, the state of the Au eutectic alloy does not matter for the growth of nanowires as long as there is a thermodynamic driving force to start and sustain the growth.

A thermodynamic driving force is essential to ensure the VLS or the VSS to take place. Firstly, to ensure the deposition of the growth species from their vapor phase to the substrate, the vapor phase has to be highly supersaturated with the growth species for them to deposit on the surface. The supersaturation ratio $\Phi_V = \left(J / J_0 \right)$ must exceed unity and is typically orders of magnitude higher, where J is the deposition rate and J_0 is the equilibrium desorption rate. Once deposition is ensured by forcing a high supersaturation of the growth species, then the growth species will nucleate on the surface or diffuse into a region with lower supersaturation. The supersaturation on the surface drops from the supersaturation in the vapor phase due to the surface nucleation and its supersaturation ratio becomes $\Phi_A = \left(n / n_0 \right)$, where n is the concentration of the growth species on the surface and n_0 is the equilibrium surface concentration of the growth species. The Au seed alloy will always be a destination for the growth species as long as Φ_A of the adatoms on the surface is higher than supersaturation ratio of the growth species in the Au

alloy $\Phi_L = \left(C / C_0 \right)$, where C is the concentration of the growth species in the Au alloy and C_0 is the equilibrium concentration of the growth species in the eutectic alloy.

The supersaturation ratios used to describe the state of the vapor, surface adatoms and liquid phase of the growth species can be substituted by the using chemical potentials, $\Delta\mu = k_B T \ln(\Phi)$. The chemical potentials $\Delta\mu_{VS}$, $\Delta\mu_{AS}$ and $\Delta\mu_{LS}$ are the difference in the chemical potentials for the vapor, adatom and liquid states, respectively, taking the solid crystalline state of the material as the reference.

The final condition to ensure nanowire growth is that $\Delta\mu_{LS}$ must exceed the nucleation barrier of the critical nucleus ΔG^* for a critical nucleus to form. In conclusion, the driving force to ensure nanowire growth is given by

$$\Delta\mu_{VS} > \Delta\mu_{AS} > \Delta\mu_{LS} > \Delta G^* \tag{1.1}$$

.

1.3 Growth Kinetics of Nanowires

The driving thermodynamic force is essential to ensure the growth of nanowires. However, it is of great importance to understand the means by which the mass is transferred to the growth site, the Au droplet. The paths of the atoms can have great impact on the morphology of the grown nanowires. Hence, the growth kinetics play an role in the growth of nanowires.

The study of the growth kinetics started with Wagner and Ellis [41]-[43]in the 1960s, when they grew Si whiskers using chemical vapor deposition (CVD). The growth of these whiskers resulted from Au impurities on a {1 1 1} Si substrate. It was explained that the mass transport took place by direct deposition of the growth species from the highly supersaturated vapor phase, directly to the liquid Au particle. The excess growth

species within the liquid alloy would then precipitate from the droplet at the liquid-solid interface, resulting in nanowire growth. The growth flux was given by:

$$J = \frac{\alpha\left(P - P_0\right)}{\sqrt{2\pi m k_B T}} \tag{1.2}$$

where J is the atoms/unit area/unit time, α is the sticking coefficient, P is the vapor pressure and P_0 is the equilibrium vapor pressure at the temperature T and k_B is the Boltzmann constant. The growth had a diameter limitation and the Gibbs-Thomson effect was used to described it,

$$R_{\min} = \frac{2\gamma_{LV}\Omega}{k_B T \ \ln(\Phi_V + 1)} \tag{1.3}$$

where $R_{\min}$ is the minimum critical radius of the droplet for growth to take place. γ_{LV} is the surface tension of the liquid-vapor interface of the Au droplet, Ω is the atomic volume of the growth species and Φ_V is the supersaturation ratio.

Givargizov-Chernov [44]-[45], in the 1970's, continued the work on Si whickers grown by CVD. Their model took into account the height dependence of these whiskers on their diameters. The critical radius described by Wagner and Ellis was not the only factor controlling the growth. They have also taken into account the decrease in whisker height, as the diameter of the whisker decreased. this was attributed to the decrease in the chemical potential of the liquid droplet as described by the Gibbs-Thomson effect

$$\Delta\mu_V = \Delta\mu_{V0} - \frac{2\gamma_{VS}\Omega}{R} \tag{1.4}$$

where $\Delta\mu_{V0}$ is the chemical potential of the growth species in the vapor phase in the case of $R \to \infty$ and γ_{VS} is the energy of the vapor-solid interface. The height of the nanowire, H_{nw}, was given by a semi-empirical formula in terms of its growth rate:

$$\frac{dH_{nw}}{dt} = b\left[\frac{\Delta\mu_{V0}}{k_B T} - \frac{2\gamma_{VS}\Omega}{k_B T}\frac{1}{R}\right]^2, \tag{1.5}$$

where *b* is a kinetic coefficient that is independent of the chemical potential, The value of *b* can be obtained from the $\sqrt{dH_{nw}/dt}$ versus $1/R$ plot, by measuring its slope. The condition of the critical radius can be derived from eq. (1.5) by equating the growth rate to zero, which yields to:

$$R_{\min} = \frac{2\gamma_{VS}\Omega}{\Delta\mu_{V0}}. \tag{1.6}$$

The modelling of nanowires growth, showed great advances in the 2000's, as interest in nanowires as futuristic devices grew. Dubrovskii et al [46]took the Givargizov-Chernov a step further to consider the supersaturation ratio of the vapor phase in comparison to that of the liquid droplet, because the nucleation take place from the liquid droplet not from the vapor phase. The growth rate of the nanowire was given by

$$\frac{dH_{nw}}{dt} = \beta(\Phi_V - \Phi_L), \tag{1.7}$$

where β is a kinetic coefficient. The model also demonstrated the difference in growth rate between the 2D surface and nanowire, and the faster growth of the nanowire was favored than the 2D surface due to the lower interfacial energy underneath the Au seed at the liquid-solid interface, compared to the 2D vapor-solid one.

The above models for nanowire growth describe the case of direct impingement of the growth species on the Au seed particle as the mean of mass transport. When using different methods of growth, such as Si using molecular-beam epitaxy (MBE) [47], the heights of the nanowires were found to be proportional to $1/R$. Further investigations on

III-V compounds have also reviled this the same behaviour. This behaviour was attributed to the diffusion of the growth species in the form of adatoms on the sidewall of the nanowire before they are gathered by the Au droplet. Modelling the direct impingement on the Au droplet and the adatom diffusion contributions to growth was given by:

$$\frac{dH_{nw}}{dt} = A + \frac{B}{R}, \tag{1.8}$$

where A and B are the parameters responsible for the direct impingement and the adatom diffusion, respectively. This model was verified by several published results [20], [38]. In addition to the $1/R$, investigations done by Johansson et al [48] examining the Gibbs-Thomson effect for InAs nanowires, revealed that its effect is insignificant on the growth of nanowires, with diameters ranging from 20-100 nms.

Experimental results showing the H_{nw} versus $1/R$ behaviour for nanowires with diameters below 120 nms, started to show slight increase in the height beyond this diameter [38]. A merge between the Givargizov-Chernov model and the diffusion induced model [49], was able to provide a universal solution to this phenomenon. The increase in length at larger diameters was attributed to the switch from a mono-nucleation regime to a poly-nucleation regime at the growth interface [51].

Since, the mass transport to the Au seed differs based on the method of growth, Dubrovskii et al [50] described a model that can be used for vapor phase deposition (VPD), such as CVD, in addition to systems with high vacuum deposition (HVD), such as MBE. The model described in Figure 1.4 can be tailored to match the HVD and the VPD growths by varying the angle α and the diffusion lengths on the substrate and along the nanowire. For example, the angle α is considered to be equal to 90º in the case of CVD along with having very short diffusion length on the substrate and the nanowire's sidewalls.

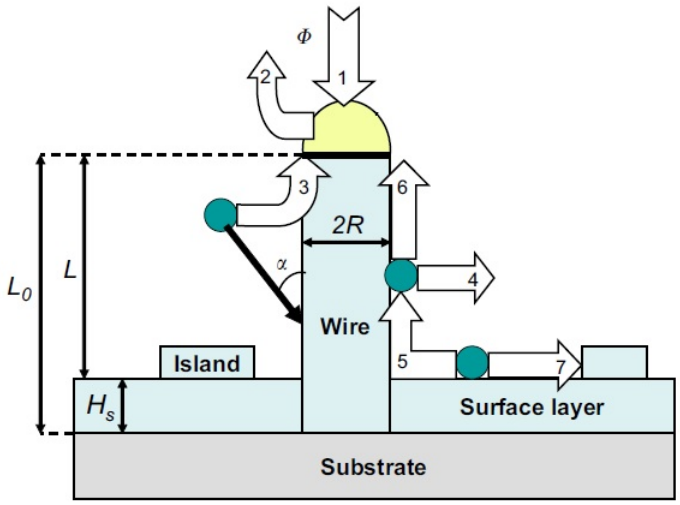

Figure 1.4: The model of wire growth: (1) direct impingement, (2) desorption from the drop, (3) diffusion flux from the sidewalls to the drop, (4) desorption from the sidewalls, (5) diffusion from the substrate to the sidewalls, (6) diffusion from the substrate along the sidewalls to the drop, (7) nucleation on the surface (Adopted from [49]).

The growth rate of the nanowires in HVD systems has been argued to be dependent on the traditional $1/R$ behaviour in addition to $1/R^2$ [50], which has been argued to be due to the feeding of adatoms for the surface of the substrate.

1.4 Crystal Structure of Nanowires

Nanowires have shown that they can exhibit crystal structures different than the normal form that the bulk material show. Although the bulk III-V materials take the cubic zinc-blend (ZB) crystal structure, their nanowire counterparts prefer the hexagonal wurzite (WZ) structure. The crystal structure for each material show dependence on the nanowire's diameter, growth temperature, rate and V/III flux ratio. Dick et al. [62] demonstrated the change in the nanowire crystal phase based on the above parameters

using metalorganic vapour phase epitaxy (MOVPE) for many III-V compounds. For example, GaAs grown with the temperature range of 350-550ºC, showed ZB phase with low density twin plans at the lower limit of the temperature range. For growths at 450ºC, the ZB nanowire started having WZ short segments as stacking faults. The nanowire phase showed the dominance of the WZ phase, which agrees with the result of Plante et al [52]that was performed in MBE with the temperature range of 500-600ºC. In addition, the experiments done by Plante et al showed increase in the WZ phase purity of the nanowires as the growth rate decreased and the V/III flux increased.

Tuning the crystal structure and perfecting the phase of the grown nanowires needs recipes for the growths that can be achieved by lot of experimentations. Interval interruptions during MBE growth of nanowire superlattices [53]succeeded in developing WZ single crystalline nanowires. Joyce et al [54], used the growth conditions to achieve pure ZB nanowires using MOCVD at low temperature and high V/III ratio and pure WZ nanowires at high temperature and low V/III ratio.

1.4.1 Modelling of Crystal Structure

Early models attributed the occurrence of the hexagonal WZ to be due to the its lower energy of formation at small diameters. Akiyama et al [55]-[56]used the hexagonal nanowire shape to calculate its energy. Their results showed, that small diameters nanowires favored the hexagonal crystal and beyond a critical crossover diameter, the crystal structure switches to the cubic zinc-blend form. Concerns were raised about this approach because the critical crossover diameter, where ZB becomes favorable over WZ, was underestimated where it was in the range of 15-20 nms.

Glas et al. [57], based their analysis on the classical nucleation theory of the growth species at the growth interface of the nanowire. For a nucleus forming at the growth interface the Gibbs-free energy of formation is given by

$$\Delta G = -(\frac{A.h}{\Omega})\Delta\mu + (P.h)\Gamma_l + A\psi \text{ ,} \quad (1.9)$$

where Ω is the volume of the nucleating atoms and $\Delta\mu$ is their chemical potential in the Au droplet. The height of the nucleus h is equivalent to one monolayer, A is the area of the nucleus = ar^2 and P is the lateral perimeter of the nucleus = pr for the lateral surface energy of the nucleus $\Gamma_l = \left[(1-\alpha)\gamma_{lL} + \alpha\gamma_{lV}\right]$. The lateral surface energies of the nucleus γ_{lL} and γ_{lV} are for the lateral sides facing the liquid and the vapor, respectively, and α is the fraction of the nucleus facing the vapor phase. The parameter ψ represents the difference in cohesive energy between the ZB and the WZ phase, given that $\psi\big|_{ZB} = 0$.

Nucleation was assumed to occur either at the triple phase line (TPL) of the Au droplet, vapor phase and nanowire, , as shown in Figure 1.5 (b), or away from that line close to the center of the growth interface, as shown in Figure 1.5 (c). Due to the excess energy needed for the WZ nucleation from the factor $A\psi$ in the above equation, nucleation away from the TPL would always be in the ZB phase. However, if nucleation is to occur at the TPL, WZ nucleation becomes more favorable if the supersaturation in the Au droplet in high. In addition, due to the elimination of part of the liquid-vapor interface during TPL nucleation, the TPL becomes energetically favorable site for nucleation.

The nucleation based model gave an explanation on why a phase would occur over the other but did not give explanation to why nanowires would have stacking faults or mixed phases. Johansson et al [58] utilized the nucleation based model and explained the occurrence of stacking faults or twin plans. In his model, the critical nucleation barrier was calculated for the WZ and the ZB phase, and were given by:

$$\Delta G_{\phi}^{*} = \frac{p^{2}}{4A} \frac{\Omega\ h \cdot \Gamma_{\phi}^{\ 2}}{\left(\Delta\mu\ - \Omega\ \psi_{\phi} / h \right)}, \tag{1.10}$$

where ϕ is the crystal phase, WZ or ZB.

A competition between the two nucleation events (WZ or ZB) would take and it would be governed by a random Poisson relation. The probability of forming the WZ can be given as:

$$P_{WZ} = \frac{\exp[-\Delta G_{WZ}^{*}]}{\exp[-\Delta G_{WZ}^{*}] + \exp[-\Delta G_{ZB}^{*}]}. \tag{1.11}$$

The Poisson nucleation process at the nanowire growth interface, was the basis for further work, where the growth kinetics were included to give a better description of the formation of phases [59]. In [60], the Gibbs-Thompson effect was included in the analysis of the model and was pointed out to be the reason for the dependence of crystal structure on nanowire diameter for InAs naowires.

A big challenge remain in the modelling the probability of crystal phases in nanowires which is the values of the surface energies between the formed nucleus and the underlying surface, the vapor phase and the liquid droplet. The values used for these surface energies are mostly fitting parameters [58]-[59], or based upon the calculation of surface states of the nucleus at the growth interface [63]. However, further investigations and experimentations are required to include the effect of supersaturation liquid droplet and the vapor phase and its effect on the interface energies.

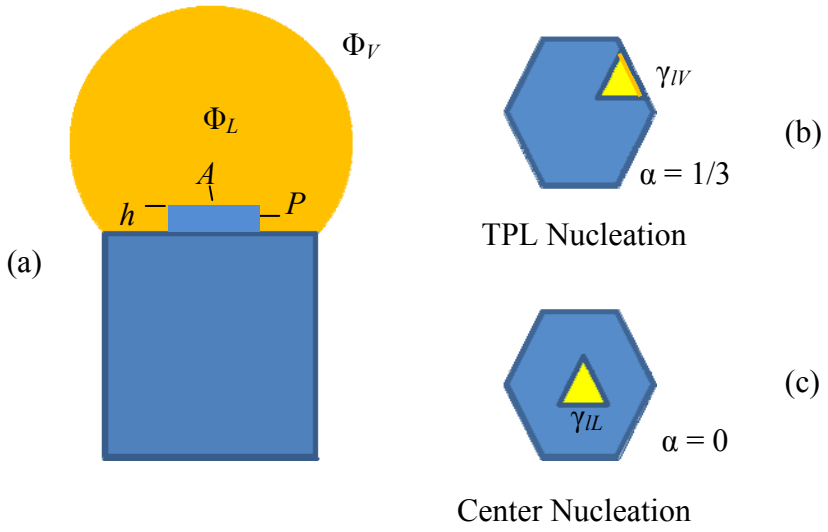

Figure 1.5: Illustration of the nucleation process (a) at the liquid-solid interface. (b) showing TPL and (c) center nucleation

1.5 Thesis Overview

The main discussion in the thesis revolve around the growth of ternary nanowires, particularly InGaP. The experimental work done on the InGaP nanowires, has directed our focus the understanding the growth aspect and their crystal structure with the help of theoretical modelling. The dissertation is divided into three main chapters. In Chapter 2, the main experimental procedures are discussed. The chapter shows the results and the characterization of ternary InGaP nanowire growths and experiments. Qualitative discussions are provided to explain our results and observations. The main highlights in Chapter 2 is the growth rate study of InGaP nanowires, where the elemental composition and the crystal structure dependence are discussed.

Chapter 3 discusses the quantitative physical-based growth model that addresses the results shown in Chapter 2. The model deals with the growth, morphology, diameter and temperature dependence and elemental distribution of the different elements along the nanowire's horizontal and vertical axis. The growth model is considered the first to explain the elemental distribution in ternary nanowires. The key approach in the model is to separate the growth species into two systems of InP and GaP. As a result, we are able to describe the discrepancies in In behaviour and its dependence on growth rate, temperature and diameter size.

Chapter 4 is focused on the change in crystal structure of the growth discussed in chapter 2 and its dependence on the growth rate. Fitting out data with the measurements have indicated that In nucleation at the growth interface promotes ZB formation, whereas Ga nucleation promotes the WZ phase nucleation. Furthermore, the dependence of the crystal structure on diameter of the seed particle was taken into consideration by modeling the surface energy of the nucleus-liquid interface as a diameter dependent.

References

[1] http://www.itrs.net/

[2] Y. Cui, X. Duan, J. Hu, and C. M. Lieber, J. Phys. Chem. B 104, 5213 (2000).

[3] X. Jiang, Q. Xiong, S. Nam, F. Qian, Y. Li, and C. M. Lieber, Nano Lett. **7**, 3214 (2007).

[4] M. J. Gilbert and S. K. Banerjee, J. Vac. Sci. Technol. B 25, 189 (2007)

[5] X. Duan, J. Wang, and C. M. Lieber, Appl. Phys. Lett. **76**, 1116 (2000).

[6] M. D. Kelzenberg, S. W. Boettcher, J. A. Petykiewicz, D. B. Turner-Evans, M. C. Putnam, E. L. Warren, J. M. Spurgeon, R. M. Briggs, N. S. Lewis & H. A. Atwater, Nat. Mater. 9, 239 (2010)

[7] Y. Huang, X. Duan, C. Lieber, emsp, and M, *Nanowires for Integrated Multicolor Nanophotonics* (WILEY‐VCH Verlag, 2005).

[8] Mu, Shi, J. C. Chang, and S.-T. Lee, Nano Letters **8**, 104 (2008).

[9] K. A. Dick, Prog. Cryst. Growth Ch. 54, 138 (2008).

[10] G. Sauer, G. Brehm, S. Schneider, K. Nielsch, R. B. Wehrpohn, J. Choi, H. Hofmaister, and U Gosele, J. Appl. Phys. 91, 3243 (2002).

[11] A. Gustafsson, F. Reinhardt, G. Biasiol, and E. Kapon, Appl. Phys. Lett. 67, 3673 (1995).

[12] P. Mohan, J. Motoshisa, and T. Fukui, Appl. Phys. Lett. 88, 013110 (2006).

[13] H. J. Fan, P. Werner, and M. Zacharais, Small 2, 700 (2006).

[14] M. E. Messing, K. Hillerich, J. Johansson, K. Deppert, and K. A. Dick, Gold Bulletin 42, 172 (2009).

[15] M. C. Plante, Ph.D. Thesis, McMaster University (2009).

[16] K. Hiruma, M. Yazawa, T. Katsuyama, K. Ogawa, K. Haraguchi, M. Koguchi, and H. Kakibayashi, Journal of Applied Physics 77, 447 (1995).

[17] B. J. Ohlsson, M. T. Bjork, M. H. Magnusson, K. Deppert, L. Samuelson, and L. R. Wallenberg, Applied Physics Letters 79, 3335 (2001).

[18] E. P. A. M. Bakkers, J. A. vam Dam, S. De Franceschi, L. P. Kouwenhoven, M. Kaiser, M. Verheijen, H. Wodergem, and P. van der Sluis, Nat. Mater. 3, 769 (2004).

[19] T. Martensson, M. Borgstrom, W. Seifert, B. J. Ohlsson, and L. Samuelson, Nanotechnology 14, 1255 (2003).

[20] L. E. Jensen, M. T. Bjork, S. Jeppesen, A. I. Persson, B. J. Ohlsson, and L. Samuelson, Nano Lett. 4, 1961 (2004).

[21] T. Martensson, P. Carlberg, M. Borgstrom, L. Montelius, W. Seifert, and L. Samuelson, Nano Letters 4, 699 (2004).

[22] B. Nikoobakht, C. A. Michaels, S. J. Stranick, and M. D. Vaudin, Applied Physics Letters 85, 3244 (2004).

[23] W. Lee, M. Alexe, K. Nielsch, and U. Gosele, Chemistry of Materials 17, 3325 (2005).

[24] H. J. Fan, W. Lee, R. Scholz, A. Dadgar, A. Krost, K. Nielsch, and M. Zacharias, Nanotechnology 16, 913 (2005).

[25] Z. H. Wu, X. Y. Mei, D. Kim, M. Blumin, and H. E. Ruda, Applied Physics Letters 81, 5177 (2002).

[26] R. Glass, M. Moller, and J. P. Spatz, Nanotechnology 14, 1153 (2003).

[27] R. Glass, M. Arnold, E. A. Cavalcanti-Adam, J. Blummel, C. Haferkemper, C. Dodd, and J. P. Spatz, New Journal of Physics 6 (2004).

[28] H. J. Fan, P. Werner, and M. Zacharias, Small 2, 700 (2006).

[29] M. H. Magnusson, K. Deppert, J. O. Malm, J. O. Bovin, and L. Samuelson, Journal of Nanoparticle Research 1, 243 (1999).

[30] C. P. T. Svensson, W. Seifert, M. W. Larsson, L. R. Wallenberg, J. Stangl, G. Bauer, and L. Samuelson, Nanotechnology 16, 936 (2005).

[31] S. A. Dayeh, E. T. Yu, and D. Wang, Nano Letters 7, 2486 (2007).

[32] V. L. Colvin, A. N. Goldstein, and A. P. Alivisatos, Journal of the American Chemical Society 114, 5221 (1992).

[33] K. C. Grabar, P. C. Smith, M. D. Musick, J. A. Davis, D. G. Walter, M. A. Jackson, A. P. Guthrie, and M. J. Natan, Journal of the American Chemical Society 118, 1148 (1996).

[34] A. Doron, E. Katz, and I. Willner, Langmuir 11, 1313 (1995).

[35] F. Burmeister, C. Schafle, T. Matthes, M. Bohmisch, J. Boneberg, and P. Leiderer, Langmuir 13, 2983 (1997).

[36] V. G. Dubrovskii, G. E. Cirlin, I. P. Soshnikov, A. A. Tonkikh, N. V. Sibirev, B. S. Yu, and V. M. Ustinov, Physical Review B (Condensed Matter and Materials Physics) 71, 205325 (2005).

[37] J. C. Harmand, G. Patriarche, N. Pere-Laperne, M. N. Merat-Combes, L. Travers, and F. Glas, Applied Physics Letters 87, 203101 (2005).

[38] M. C. Plante and R. R. LaPierre, Journal of Crystal Growth 286, 394 (2006).

[39] S. Kodambaka, J. Tersoff, M. C. Reuter, and F. M. Ross, Science **316**, 729 (2007).

[40] K. A. Dick, K. Deppert, T. Martensson, B. Mandl, L. Samuelson, and W. Seifert, Nano Letters **5**, 761 (2005).

[41] R. S. Wagner and W. C. Ellis, Appl. Phys. Lett. 4, 89 (1964).

[42] R. S. Wagner, W. C. Ellis, K. A. Jackson, and S. M. Arnold, J. Appl. Phys. 35, 2993 (1964).

[43] R. S. Wagner and W. C. Ellis, Trans. Metal. Soc. AIME 233, 1053 (1965).

[44] E. I. Givargizov, J. Cryst. Growth 31, 20 (1975).

[45] E. I. Givargizov and A. A. Chernov, Kristallografiya 18, 147 (1973).

[46] V. G. Dubrovskii and N. V. Sibirev, Phys. Rev. E 70, 031604 (2004).

[47] L. Schubert, P. Werner, N. D. Zakharov, G. Gerth, F. M. Kolb, L. Long,U. Gosele, and T. Y. Tan, Appl. Phys. Lett. 84, 4968 (2004).

[48] J. Jonas, A. W. Brent, A. D. Kimberly, and S. Werner, Nanotechnology, S355 (2006).

[49] V. G. Dubrovskii and N. V. Sibirev, Journal of Crystal Growth 304, 504 (2007).

[50] V. G. Dubrovskii, N. V. Sibirev, R. A. Suris, G. E. Cirlin, J. C. Harmand, and V. M. Ustinov, Surface Science 601, 4395 (2007).

[51] D. Kashchiev, Crystal Growth & Design **6**, 1154 (2006).

[52] M. C. Plante and R. R. LaPierre, Nanotechnology, 495603 (2008).

[53] P. Mohseni , K and R. R. LaPierre, Nanotechnology, 025610 (2009).

[54] H. J. Joyce, J. Wong-Leung, Q. Gao, H. H. Tan, and C. Jagadish, Nano Letters **10**, 908 (2010).

[55] T. Akiyama, K. Nakamura, and T. Ito, Physical Review B (Condensed Matter and Materials Physics) **73**, 235308 (2006).

[56] T. Akiyama, K. Sano, K. Nakamura, and T. Ito, Japanese Journal of Applied Physics **45**, L275 (2006).

[57] F. Glas, J.-C. Harmand, and G. Patriarche, Physical Review Letters **99**, 146101 (2007).

[58] J. Johansson, L. S. Karlsson, K. A. Dick, J. Bolinsson, B. A. Wacaser, K. Deppert, and L. Samuelson, Crystal Growth & Design **9**, 766 (2009).

[59] V. G. Dubrovskii, N. V. Sibirev, J. C. Harmand, and F. Glas, Physical Review B (Condensed Matter and Materials Physics) **78**, 235301 (2008).

[60] J. Johansson, K. A. Dick, P. Caroff, M. E. Messing, J. Bolinsson, K. Deppert, and L. Samuelson, The Journal of Physical Chemistry C **114**, 3837 (2010).

[61] P. Caroff, K. A. Dick, JohanssonJ, M. E. Messing, DeppertK, and SamuelsonL, Nat Nano **4**, 50 (2009).

[62] K. A. Dick, P. Caroff, J. Bolinsson, M. E. Messing, J. Johansson, K. Deppert, L. R. Wallenberg, and L. Samuelson, Semicond. Sci. Technol. **25** (2010).

[63] N. V. Sibirev, M. A. Timofeeva, A. D. Bol'shakov, M. V. Nazarenko, and V. G. Dubrovskiĭ, Physics of the Solid State **52**, 1531 (2010).

Chapter 2

Dependence of InGaP Nanowire Morphology and Structure on Molecular Beam Epitaxy Growth Conditions

Semiconductor nanowires (NWs) have been intensely explored over the past decade for next generation lasers [1], light-emitting diodes (LEDs) [2], [3], sensors [4], photovoltaic devices [5], single electron transistors [6], and photodetectors [7]. NWs can be self-assembled using metal-assisted growth which was first introduced as the vapor-liquid-solid (VLS) mechanism by Wagner and Ellis [8]. In the VLS process, a metal catalyst (typically Au) acts as a collecting agent for reactants resulting in site-selective growth of NWs. Various deposition techniques have been employed for NW synthesis, such as metalorganic vapor phase epitaxy (MOVPE) [9] and molecular beam epitaxy (MBE) [10, 11].

Many device applications require heterostructures containing III-V compound semiconductors such as GaAsP for near-infrared lasers [1], InGaP for LEDs [3], InAsP for infrared photodetectors [7] and quantum dot LEDs [2], and InGaAs for field-effect transistors [6]. Recently, numerous efforts have demonstrated the photovoltaic capabilities of III-V semiconductor NWs [5] where InGaP might be incorporated in a multi-junction design to improve energy conversion efficiency. Despite this, comparatively little work has been performed to understand the growth of ternary III-V compound semiconductor NWs as compared to elemental NWs such as Si, Ge and binary

III-V NWs. In this paper, we focused on the morphology, composition, and crystal structure of InGaP NWs.

One of the main challenges lies in controlling the morphology (length, diameter, and shape) and crystal structure of NWs. Depending on growth conditions (temperature, impingement rates, and V/III flux ratio), NWs may grow axially by the VLS mechanism or radially by vapor-solid deposition on the NW sidewalls. Semiconductor NWs typically exhibit the hexagonal wurtzite (WZ) structure, unlike the usual cubic zincblende (ZB) structure that occurs in their bulk state [11], [12]. Insertions of a few monolayers of ZB stacking typically occur along the length of NWs, affecting their electrical and optical properties [13, 14]. In this paper, a growth study is performed on InGaP NWs to show the control of morphology and stacking fault density with flux conditions. The results show that stacking faults can be nearly eliminated by using the proper growth conditions. A natural core-shell structure is also formed whereby the In content is greater near the NW centre. A qualitative explanation is provided to understand these observations.

2.1 Experimental Details

NWs were grown on n-type (111) B-oriented GaAs substrates. Prior to NW growth, the substrates were subjected to UV ozone oxidation for 20 minutes followed by a 30 second etch in HF and a deionized water rinse for 5 minutes to remove surface hydrocarbons. After cleaning, a 1 nm thick gold film was deposited on the substrates at room temperature by e-beam evaporation. The samples were then transported in ambient air to a gas source molecular beam epitaxy (GS-MBE) system for NW growth. In GS-MBE, group III elements are supplied from elemental effusion cells while group V species are supplied as dimers (As_2, P_2) from cracking of hydrides (AsH_3, PH_3). Before growth was initiated, the samples were heated to 550 °C for 10 minutes under hydrogen plasma and As_2 flux to desorb surface oxides. The Au film, when annealed in the MBE,

provided the necessary seeds for the Au-assisted growth of the NWs. The substrate temperature was then dropped to the growth temperature of 430 °C, the P_2 flux was initiated and As_2 flux terminated, and NW synthesis begun by opening the Ga and In effusion cell shutter. The composition was nominally $In_{0.5}Ga_{0.5}P$ as determined by prior thin film calibrations.

Four NW samples were grown at 430 °C referred to as samples A, B, C, and D. Samples A, B and C were grown with a group III (In and Ga) impingement rate corresponding to 2-D equivalent growth rates of 2 μm/h, 1 μm/h and 0.25 μm/h, respectively, and the growth durations were 10 min, 20 min and 80 min, respectively. Therefore, the group III impingement rate and growth duration were adjusted such that all the samples received identical group III material supply. The V/III flux ratio of these three samples was set at 1.75. Sample D was grown with conditions similar to sample C, but with the V/III flux ratio increased to 8. The growth conditions of the four samples are summarized in Table 2.1.

The morphology of the NWs was characterized using a JEOL JSM-7000F field emission scanning electron microscope (SEM). The NWs were prepared for transmission electron microscopy (TEM) measurements by a sonication method described previously [10]. SEM observations of the substrate after the sonication procedure confirmed that the NWs broke from the substrate at their bases. NW cross-sections were also prepared using an ultra-microtoming procedure. The crystal structure of the NWs was investigated using a Philips CM12 conventional TEM. Compositional analysis was performed using a JEOL JEM-2010F high resolution scanning TEM, which was equipped with energy dispersive x-ray spectroscopy (EDX).

Table 2.1 Growth conditions for samples used in this study.

Sample	Group-III impingement rate (μm/h)	Growth duration (minutes)	V/III flux ratio
A	2	10	1.75
B	1	20	1.75
C	0.25	80	1.75
D	0.25	80	8

2.2 Results

The morphology of the NWs was first surveyed by cross-sectional SEM as shown in Figure 2.1 for the four samples A-D. The NWs exhibited mostly a pencil-like shaped morphology as described previously [10], [11], where the NW diameter was nearly constant along its entire length except near the NW tip where the diameter dramatically decreased. We previously attributed this pencil-shaped morphology to radial vapor-solid growth which uniformly increases the diameter of the NWs in a layer-by-layer fashion due to deposition on the NW sidewalls [10], [11]. The radial growth of the NWs was quantified by measuring the full width at half-length, *w*, of the NWs in comparison with the Au seed diameter, *d*, from measurements on 40-50 individual sonicated NWs in TEM, such as those shown in Figure 2.2. The average *w/d* ratio of the NWs was 3, 4.3, 5 and 12 for samples A through D, respectively. Radial growth on the sidewalls of the NWs

therefore increased somewhat as the group III impingement rate decreased (comparing samples A, B, and C), but increased more substantially as the V/III ratio increased (comparing samples C and D). This effect will be discussed further in the Discussion section.

The relationship between NW length and Au particle seed diameter was also determined by direct measurement of sonicated NWs by TEM as plotted in Figure 2.3. Smaller Au seed diameters typically resulted in greater NW lengths. This trend is most obvious for sample D in Figure 2.3(d) where NW heights were greater compared to samples A-C (as discussed below). This inverse relationship between NW height and Au seed diameter is a signature of adatom diffusion along the substrate and NW sidewalls to the growing interface [15]. Also noteworthy was the disparity in NW heights among samples A-D. Sample D exhibited NW heights almost twice as great compared to the other samples for Au seed diameters below 20 nm. Therefore, in addition to showing greater radial growth, sample D also showed significantly greater axial growth in comparison to the NWs grown at lower V/III flux ratio. This effect will also be discussed further in the Discussion section.

Next, we considered the structural analysis of the NWs as measured by TEM. Figure 2.2 shows typical bright-field TEM images along the [2 -1 -1 0] zone axis for representative NWs from samples A-D. A representative selected area electron diffraction pattern, shown in the lower left corner of Figure 2.2(a) for the mid-section of sample A, indicated a wurtzite (WZ) crystal structure. The same WZ crystal structure was observed along the entire NW length, as well as for the other samples B-D. The dark and light bands intersecting the NWs in Figure 2.2 indicated the recurrence of stacking faults along the NW length as described previously for GaAs NWs [10, 11]. The stacking faults consist of a few monolayers of zincblende (ZB) crystal structure inserted periodically within the primarily WZ crystal structure of the NW. Sample A showed the

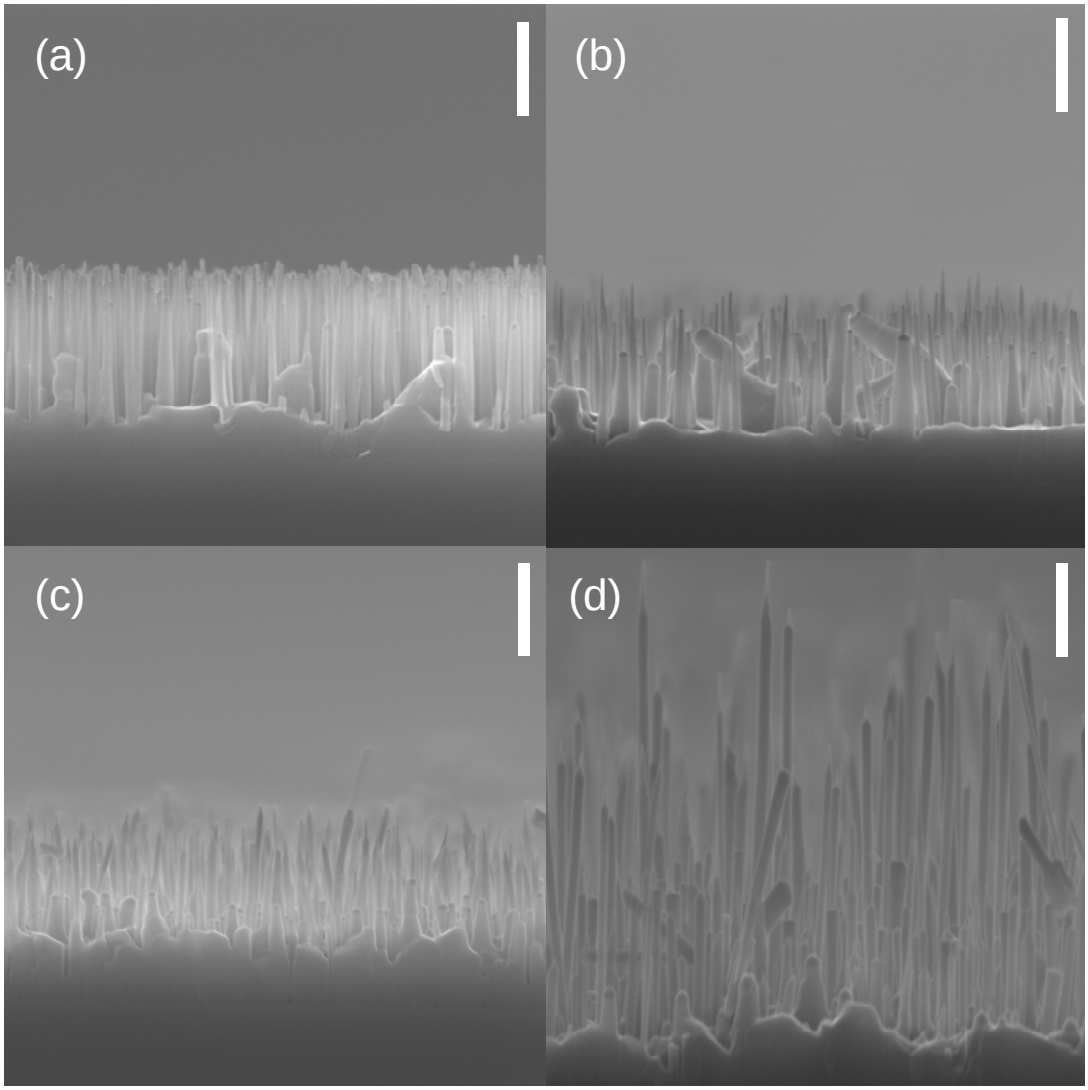

Figure 2.1 Cross-sectional SEM images of NWs for sample (a) A, (b) B, (c) C, and (d) D. Length bars indicate 500 nm

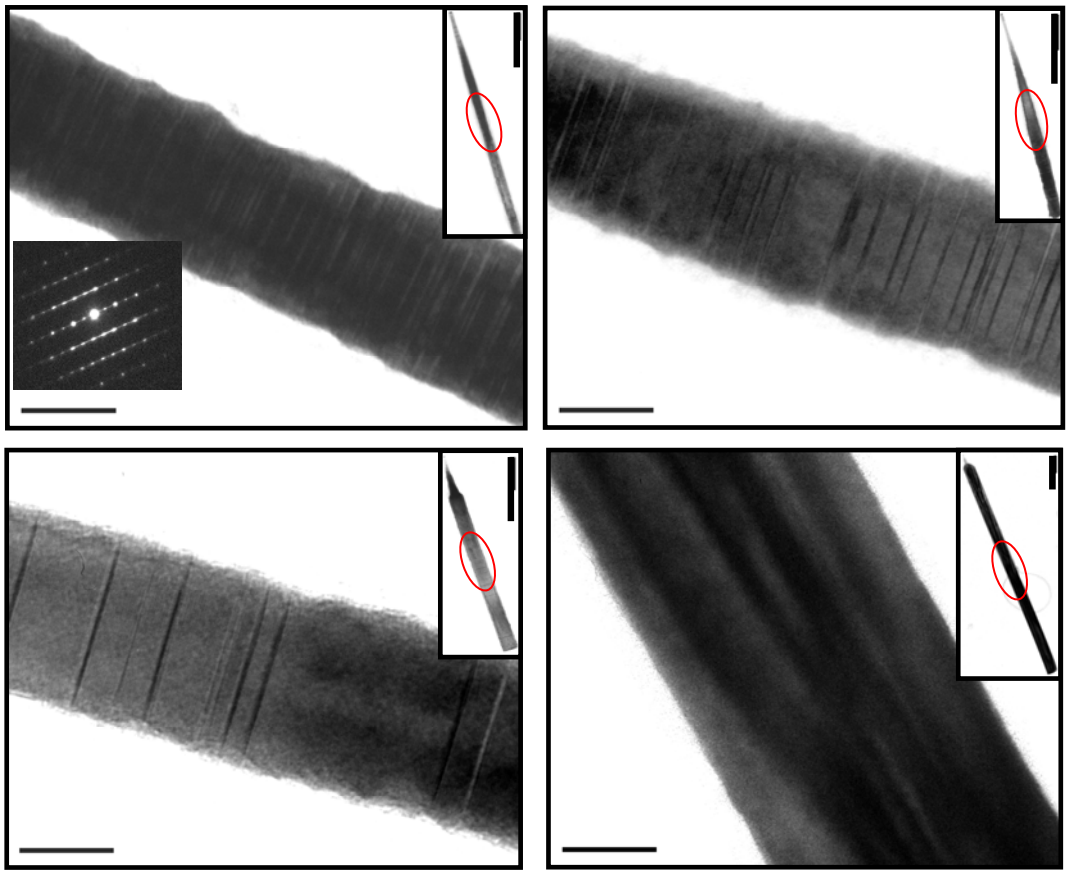

Figure 2.2 Bright-field TEM images along the [2 -1 -1 0] zone axis showing the recurrence of stacking faults along the mid-sections (i.e., half-length) of NWs for sample (a) A, (b) B, (c) C, and (d) D. Length bars indicate 20 nm. Insets in upper right show the entire nanowire. Circled regions in the insets correspond to the magnified views (inset scale bars are 200 nm). Inset at lower left of (a) indicates the selected area electron diffraction pattern near the middle of NW A indicative of the wurtzite crystal structure.

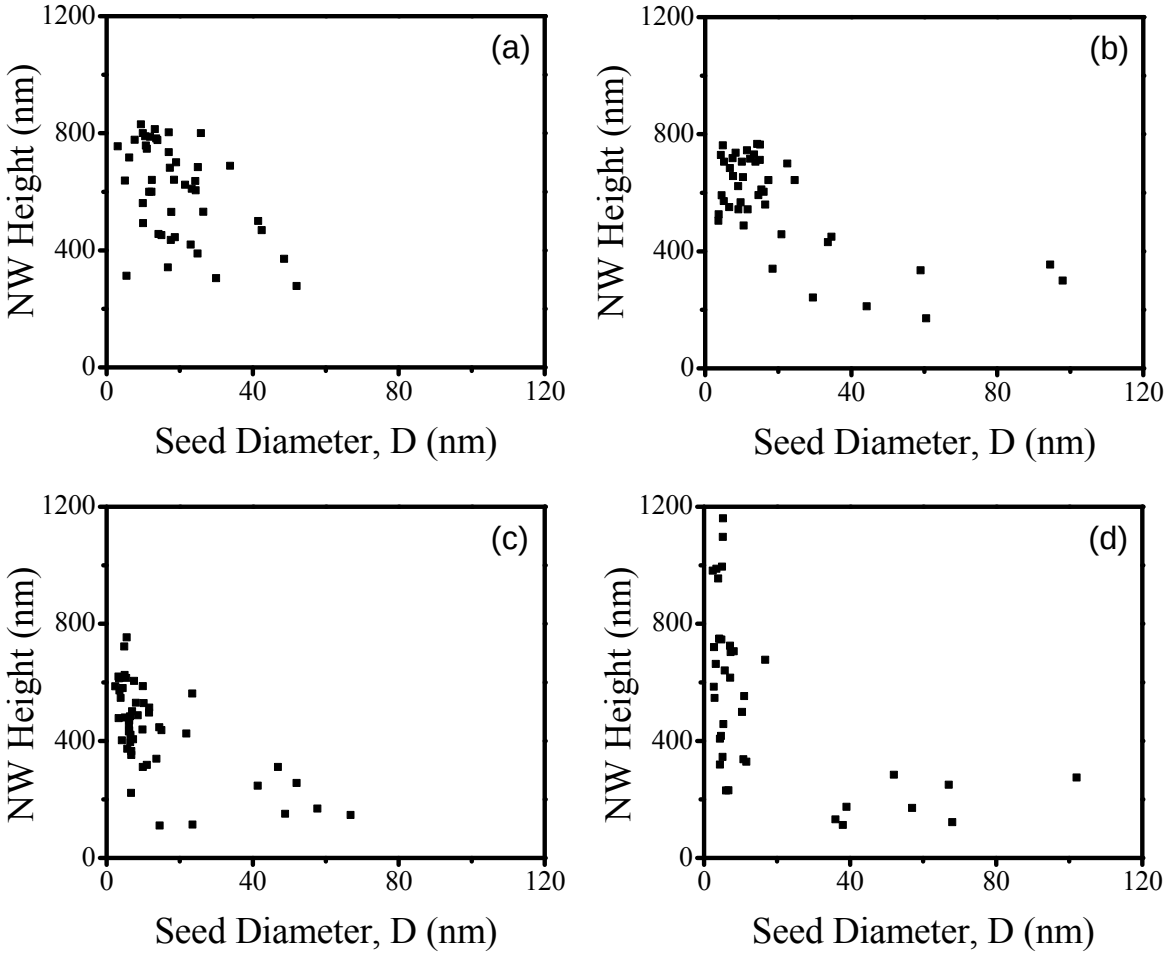

Figure 2.3 The height of each NW versus the diameter of its Au seed particle for sample (a) A, (b) B, (c) C and (d) D.

highest recurrence of stacking faults, with an average stacking fault density (SFD) measured at its mid-section (i.e., its half-length) of 0.33 nm^{-1}. Sample B indicated a lower value of the SFD compared to sample A with an average of 0.23 nm^{-1}. The SFD decreased further in sample C with an average value of 0.06 nm^{-1}. Therefore, the SFD progressively decreased as the group III impingement rate decreased from sample A to C. Sample D was grown with the identical impingement rate as sample C, but with a V/III flux ratio of 8 as compared to 1.75. Sample D exhibited from 2 to 20 stacking faults along the entire NW length with some NW mid-sections completely fault-free (as shown in Figure 2.2(d)), which was much less than the SFD of sample C. Therefore, the SFD also decreased with increasing group V impingement rate (increasing V/III flux ratio).

The elemental distribution of the four samples was investigated using EDX. All EDX profiles in Figures 2.4 and 2.5 were normalized to represent absolute composition measurements where the EDX profile for P represents 50 at% as expected for InGaP. Note that the In, Ga, and P counts decreased near the tip of the NW due to the decrease in material volume associated with the tapered morphology. Axial EDX profiles are shown in Figure 2.4(a) and (b) for representative NWs from sample A with relatively small (4 nm) and large (10 nm) Au seed particle diameter, respectively. The EDX profiles indicated much lower In compared to Ga incorporation in the NWs. Comparing Figure 2.4(a) and (b), this reduction in In incorporation compared to Ga was more severe in NWs of smaller Au particle size. Similar dependence of In content with particle size was observed among all the samples A-D.

Figure 2.5 shows axial EDX profiles for representative NWs from samples B, C and D. To evaluate differences in In and Ga incorporation among the samples B-D, EDX profiles were measured from NWs of similar Au seed diameters (5 to 6 nm) and NW diameters (36 to 50 nm). Comparing NWs from samples B and C with similar Au and NW diameters indicated increasing In incorporation as the group III impingement rate increased at constant V/III ratio. Similarly, comparing NWs from samples C and D indicated increasing In incorporation as the group V impingement rate (i.e., V/III flux

ratio) increased at constant group III impingement rate. Based on our observations on the Au particle size dependence as represented in Figure 2.4, the small difference in Au particle size (all within 1 nm) in Figure 2.5 is not sufficient to account for the observed

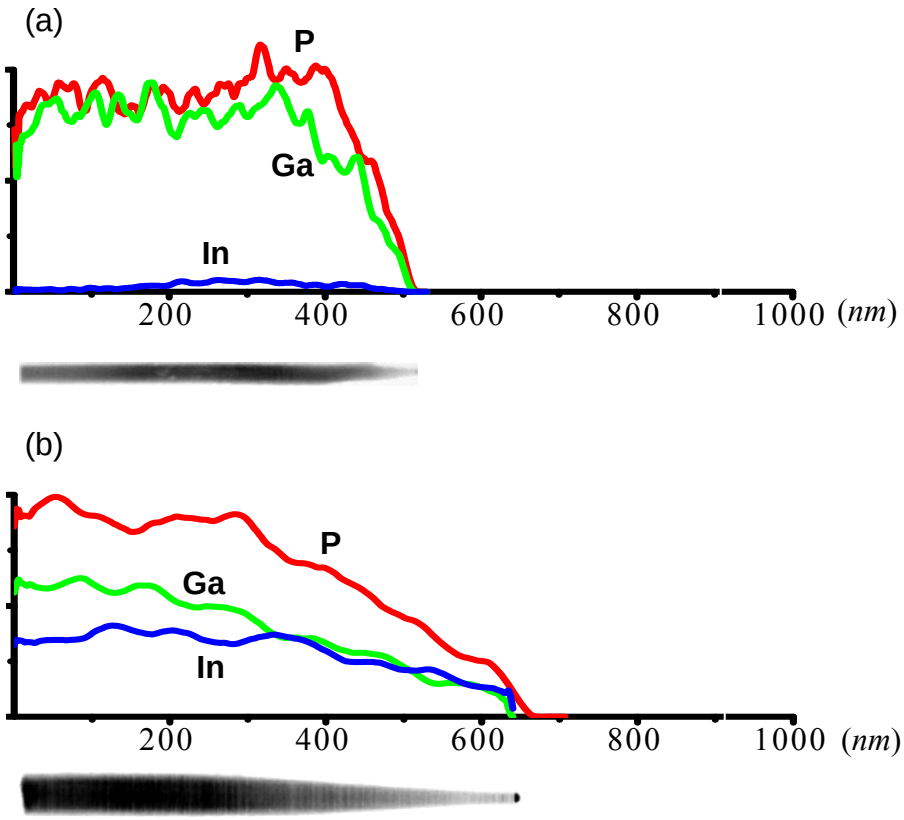

Figure 2.4 Axial EDX profiles for NWs from sample A with Au seed diameter of (a) 4 nm and (b) 10 nm, showing elemental distributions for In (blue), Ga (green) and P (red). Bright-field images of the NWs are shown below each EDX profile

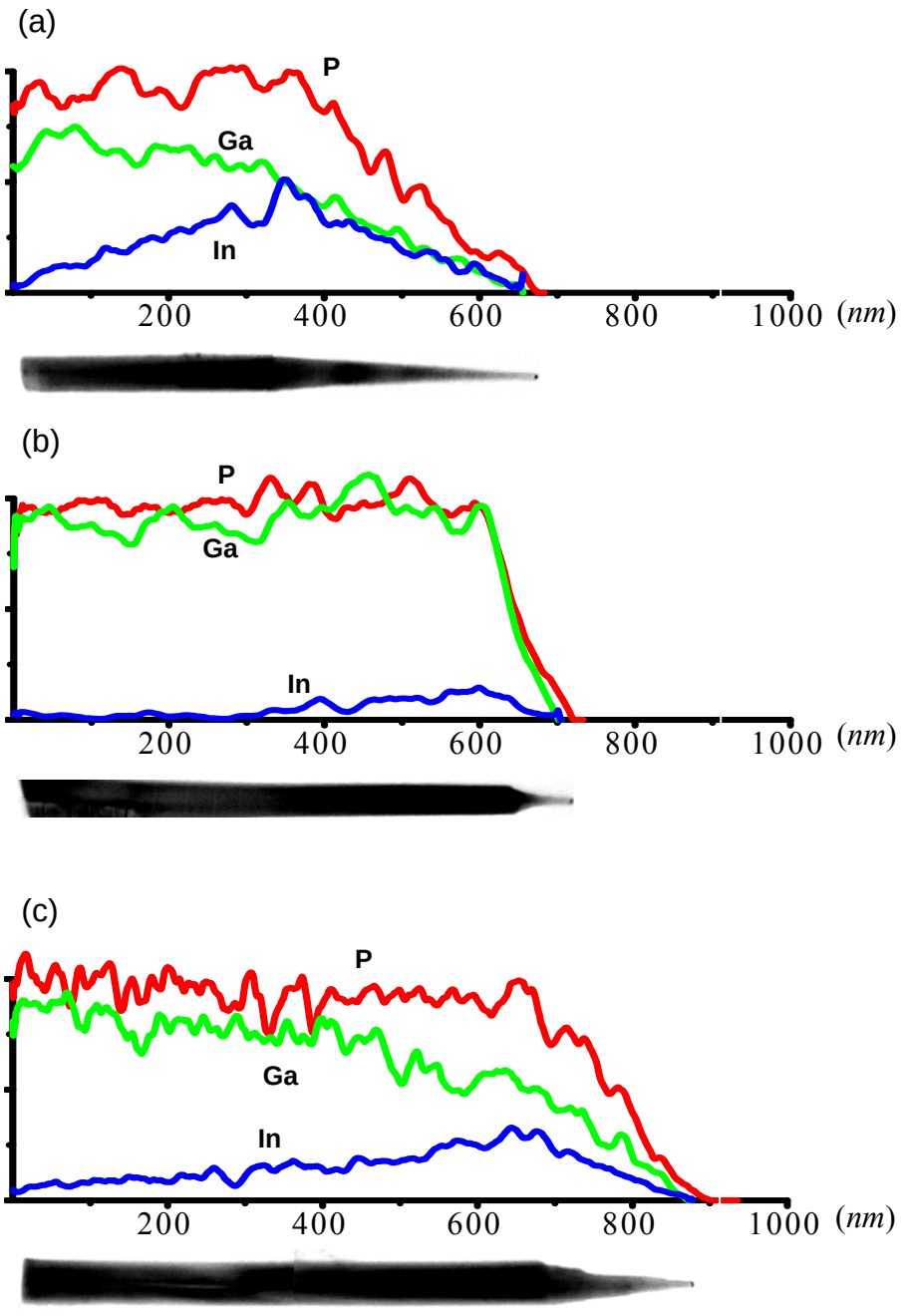

Figure 2.5 EDX profiles along the length of representative NWs from sample (a) B, (b) C and (c) D, showing elemental distributions for In (blue), Ga (green) and P (red). Bright-field images of the NWs are shown below each EDX profile.

compositional changes with growth conditions. Instead, observations among NWs with similar Au particle diameter indicated a strong dependence on group III and V impingement rate. The axial EDX profiles also indicated increasing In content along the length of the NWs. The In content typically increased toward the tip of the NW until the tapered region was reached, at which point the In counts declined due to the reduction in material volume associated with the tapered morphology of the NWs. This latter effect is described further in the Discussion section.

To further understand the three-dimensional distribution of elements within the NWs, EDX profiles were superimposed on TEM images of microtomed samples (NW cross-sections) as shown in Figure 2.6 for sample D. The cross-section of the NWs showed a hexagonal sidewall geometry with {-2 1 1 0} type facets, typical of NWs with significant radial growth [10, 11]. The EDX analysis of the microtome specimens revealed an inhomogeneous distribution of In and Ga in the NWs. First, a comparison of Figures 6(a), (b), and (c) confirmed that the In concentration increased from the bottom to the top of the NWs as described earlier for the axial EDX profiles of Figure 2.5. Absolute EDX composition measurements at the centre (core) of the NWs in Figure 2.6 indicated 15, 22, and 28 at% In at the bottom, middle, and top of the NWs, respectively, with a concomitant decrease in Ga content along the NW length. A similar decrease in Ga content along the NW length can be observed in the axial EDX profiles of Figure 2.5 in the non-tapered regions of the NWs. Second, where there is significant In concentration in the NW (i.e., near the top or midsection of the NWs), the EDX profiles clearly indicated lower In content near the surface of the NW (the edge of the microtome disk) while the Ga profile indicated a peak concentration near the surface of the NW (note the double humped behavior of Ga in Figures 6(a) and (b)). This accumulation of In near the core of the NW was confirmed by high angle annular dark field (HAADF) images. For example, the HAADF image in Figure 2.6(b) indicated a darker contrast along the

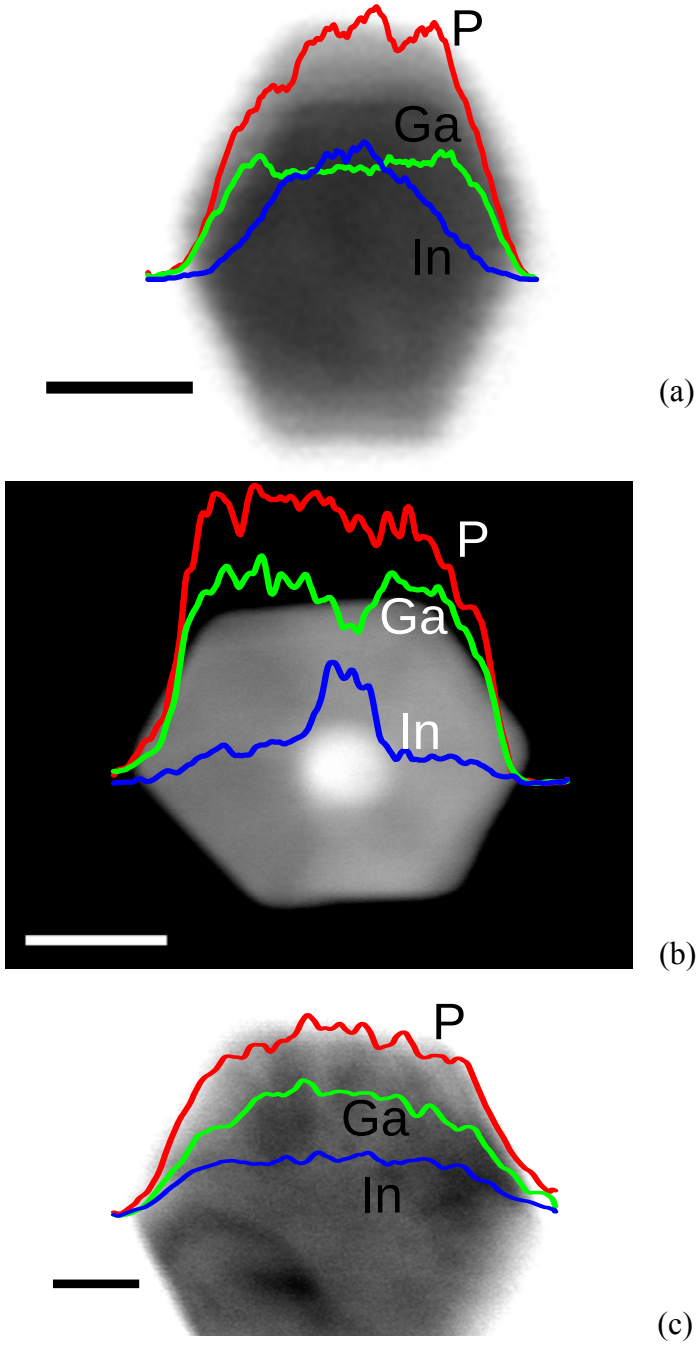

Figure 2.6 EDX radial profiles along microtomed discs from sample D showing In (blue), Ga (green) and P (red) elemental distributions superimposed on (a) bright-field TEM image near a NW top, (b) HAADF image near a NW mid-section, and (c) bright-field TEM image near a NW bottom. Length bars indicate 20 nm.

periphery of the NW which is indicative of a Ga-rich shell, consistent with the radial EDX profile (lower atomic number elements provide darker contrast in HAADF images). These results indicate that In incorporation occurs preferentially near the centre of the NW most likely by the Au-assisted process, while Ga incorporation appears to occur preferentially on the NW sidewalls by the vapor-solid process.

2.3 Discussion

Morphology

The axial growth of NWs by MBE is primarily due to the diffusion of adatoms from the substrate and along the NW sidewalls where they reach the Au seed particle and nucleate at the growth interface. The tapering of the NWs indicates the presence of radial growth due to the nucleation of adatoms on the NW sidewalls [10, 11]. Sample D, which was grown at the higher V/III flux ratio compared to samples A-C, had the greatest radial growth. This can be explained by a reduction in the diffusion length of group III adatoms on the NW sidewalls due to the presence of reactive group V dimers, which promotes sidewall nucleation.

Sample D, which was grown with the higher V/III ratio, also showed a significantly greater height of the NWs suggesting the VLS mechanism in the Au seed particle occurs under group V limited conditions. Thin film deposition by MBE normally occurs under group V rich conditions (i.e., with a V/III flux ratio greater than unity). Under these conditions, the growth rate is determined by the group III impingement rate, and any group V species in excess of group III are desorbed. However, owing to differences in group III and V adatom diffusion lengths and solubility in Au, V/III ratios ≤ 1 may prevail locally at the Au-NW interface. On this basis, the change in group III

impingement rate, while keeping the V/III ratio constant, had little effect on the axial growth of the NWs as shown in Figure 2.1(a) to (c). A similar dependence of NW axial growth with V/III ratio, and postulation of group V limited growth, has been made for MBE-grown GaAs NWs [16], [17], MBE-grown GaN NWs [18], and MOVPE-grown GaSb NWs [19].

Elemental Distributions

EDX and TEM analysis of the NWs indicated In incorporation was concentrated in the centre of the NW, while a Ga-rich shell formed from vapor-solid deposition. The development of this core/shell structure might be explained by the differences between Ga and In adatom diffusion lengths. It is well known that the Ga diffusion length is less than the In diffusion length [20-22]. Therefore, as the NW height exceeds the Ga diffusion length, limited amounts of Ga as compared to In would be able to reach the top of the NWs to contribute to axial growth. Instead, Ga will deposit on the NW sidewalls resulting in Ga enrichment in a radially grown shell. A similar effect has been observed in other ternary NW material systems. For example, a core-shell structure was observed in AlGaAs NWs where the greater diffusion length of Ga compared to Al resulted in Ga enrichment near the centre of the NW [23]. Similarly, P enrichment has been observed near the centre of GaAsP NWs due to the longer diffusion length of P compared to As [24]. The decline in Ga composition along the length of the NWs as observed in Figures 5 and 6 allow an estimation of the Ga diffusion length to be less than the maximum NW height of ~1.6 μm in sample D. However, besides the different diffusion lengths of In and Ga on the NW sidewalls, we cannot discount other competitive effects between In and Ga incorporation. Johansson et al. [25], for example, suggested that In in the Au particle suppresses the solubility of Ga. The Gibbs-Thomson effect, described below, may also significantly affect the relative incorporation of In as compared to Ga.

Despite the relatively higher In content in the core of the NW as compared to the periphery, the EDX results showed lower overall In incorporation as the Au seed particle diameter diminished. This observation may be understood by considering the arrival rate, R, of adatoms at the Au-nanowire interface [26], [27]:

$$R = \frac{P - P_\infty \exp(2\sigma\Omega_l / r_w k_B T)}{\sqrt{2\pi m k_B T}} \qquad (2.1)$$

where k_B is Boltzmann's constant, T is the growth temperature, P is the reactant pressure surrounding the NW, r_w is the Au alloy particle radius (~NW radius), σ is the vapor-liquid surface energy of the particle, Ω is the atomic volume of the reactant element in the Au particle, m is the mass of the reactant species, and P_∞ is the reactant pressure in a particle of infinite radius of curvature. The second term in the numerator of Eq. (2.1) describes the Gibbs-Thomson (GT) effect whereby smaller Au alloy particles exert a greater vapor pressure. Owing to the low supersaturations operable during MBE and the small nanoparticle sizes (<10 nm) used in this study, reactant incorporation, such as In, may be suppressed. On the other hand, considering the higher surface energy for Ga compared to In (σ~0.72 Jm^{-2} versus 0.565 Jm^{-2}, respectively [28]) means that, according to Eq. (2.1), any decrease in incorporation due to the GT effect should be greater for Ga compared to In.

Apart from the GT effect, another relevant effect is the different eutectic melting temperatures for In-Au and Ga-Au alloys, which are 454 °C and 339 °C, respectively [29], compared to our growth temperature of 430 °C. Therefore, there has been some debate whether NW growth occurs by the VLS process or the alternative vapor-solid-solid (VSS) mechanism [30]. A related consideration is therefore the different pathways for incorporation of the reactants, whether by bulk diffusion through the Au particle or

diffusion at the Au-NW interface. A recent study suggested that In may prefer bulk diffusion while Ga may incorporate by both pathways (bulk and interface diffusion) [28]. Therefore, the incorporation of In and Ga may differ substantially depending on growth conditions. Furthermore, Glas et al. [31] showed that nucleation occurs preferentially at the triple-phase line where interfacial and surface tensions may differ for In and Ga nucleation, though precise parameter values are lacking.

The observation of higher In incorporation in NWs grown with higher group III or V impingement rate may be explained by the increased supersaturation of the Au alloy where the relevance of the GT effect decreases. NWs were also grown with identical conditions as sample B but at a higher growth temperature of 490 °C. In this case, no In was observed in the NWs consistent with a lower supersaturation existing at the higher growth temperature. Finally, we note that EDX measurements of 3-4 nm diameter Au particles indicated no presence of In, while >10 nm diameter particles showed 25-35 at.% In, which again is consistent with the GT effect operating at smaller Au particles.

A more subtle effect in our study was the observed increase of In toward the top of the NWs as shown in the axial EDX profiles. This phenomenon might be explained by an increase in supersaturation as growth proceeds. A transient phase may be present in the initial stage of growth where the supersaturation of In and Ga (and possibly P) in the Au alloy is less at the beginning of growth compared to later stages of wire growth [31]. When the growth fluxes are turned on, the supersaturation, and therefore the In content, may increase until steady-state is achieved. In addition, if Ga competes with In solubility as suggested by Johansson et al. [25], then In supersaturation may increase as Ga content in the Au particle diminishes with NW length (as the NW length exceeds the diffusion length of Ga as discussed above).

Crystal Structure

Many efforts have been directed to understand the polytypism in NWs and the recurrence of stacking faults. Akiyama et al. [32, 33] attributed the WZ phase formation in NWs to the lower surface energy of the WZ phase when compared to ZB at small NW diameters. However, the estimated cross-over diameter between WZ and ZB NWs was underestimated, as WZ NWs with diameters much larger than those predicted have been reported in the literature. Later, Glas et al. [31] described the formation of different phases in NW growth by the nucleation process at the growth interface. Their analysis revealed that nucleation at the Au-NW interface was favored at the triple phase line. Johansson et al. [25] used these findings to develop a model to estimate the probability of stacking fault formation versus supersaturation. Further analysis was performed by Dubrovskii et al. [34, 35] to calculate the critical radii that allow NW formation and the radii that would favor WZ formation over ZB for a variety of III-V compounds. Based on these models, it is generally accepted that high group III supersaturation of the Au particle favors WZ while low supersaturation favors ZB. These models do not consider the influence of group V species, and instead define supersaturation relative to the group III species.

Diffraction analysis showed that all NWs in our study had the WZ crystal structure, with insertions of short ZB segments as stacking faults (except sample D which was nearly stacking fault-free). Comparing samples A to D indicated that SFD decreased as the group III impingement rate decreased and as the group V impingement rate (i.e., V/III ratio) increased. Promotion of the WZ phase with a low density of stacking faults upon lowering of the group III impingement rate (lower In and Ga supersaturation) as observed in our study is not predicted by current models, although it is in agreement with similar observations made for GaAs [11], GaP [36] and InP NWs [37]. The observed decrease in stacking fault density at high V/III flux ratio (sample D) suggests that a high group V supersaturation at the particle is also desired for crystallization in the WZ structure, as observed also in GaAs [11, 17] and InP NWs [37, 38]. Note that a prior

study indicated the possible solubility of group V species in Au during NW growth [39]. Therefore, group V supersaturation may play an important role in stacking fault formation, especially considering the possible group V limited nature of the NW growth discussed earlier. Joyce et. al. [17] speculated that As species may decrease the incidence of twin defects (or stacking faults) by reducing surface and interfacial tensions.

We also observed lower SFD in all samples A-D with smaller Au particle diameter. Although the latter observation will be the focus of another publication in the near future, we simply note here that these results have also been obtained for binary NWs including GaAs [40], InP [37, 38], and InAs [41].

2.4 Conclusions

InGaP NWs showed inhomogeneous distribution of In and Ga, with higher In content in the core of the NWs. This observation was explained by the different adatom diffusion lengths for In and Ga. Such self-assembled core-shell structures will have larger bandgaps at the NW periphery, which may have useful applications where carrier confinement in the core of the NW is required. A difference in In and Ga content was also observed, where we speculated on the influence of the GT effect, and different incorporation pathways and kinetics. The GT effect appeared to diminish with higher group III or V impingement rates due to higher supersaturation. Near elimination of stacking faults was also observed at lower group III and higher group V impingement rates. Understanding of these growth processes will require further clarification on the various kinetic and thermodynamic aspects of the NW growth including nucleation and diffusion processes. Nevertheless, our observations on the influence of growth conditions on the ternary InGaP morphology and stacking fault density was consistent with similar

observations made on simpler binary NWs, indicating common underlying growth processes.

References

[1] B. Hua, J. Motohisa, Y. Kobayashi, S. Hara, and T. Fukui, Nano Lett. 9 (2009) 112.

[2] E.D. Minot, F. Kelkensberg, M.v. Kouwen, J.A.v. Dam, L.P. Kouwenhoven, V. Zwiller, M.T. Borgstrom, O. Wunnicke, M.A. Verheijen, and E.P.A.M. Bakkers, Nano Lett. 7 (2007) 367,

[3] C.P.T. Svensson, T. Martensson, J. Tragardh, C. Larsson, M. Rask, D. Hessman, L. Samuelson, and J. Ohlsson, Nanotechnology 19 (2008) 305201.

[4] L. Mu, S. Wensheng, J.C. Chang, and S.-T. Lee, Nano Lett. 8 (2008) 104.

[5] J.A. Czaban, D.A. Thompson, R.R. LaPierre, Nano Lett. 9 (2009) 148.

[6] J. Noborisaka, T. Sata, J. Motohisa, S. Hara, K. Tomioka, and T. Fukui, Jpn. J. Appl. Phys. 46 (2007) 7562.

[7] H. Pettersson, J. Tragardh, A.I. Persson, L. Landin, D. Hessman, and L. Samuelson, Nano Lett. 6 (2006) 229.

[8] R.S. Wagner and W.C. Ellis, Appl. Phys. Lett. 4 (1964) 89.

[9] W. Seifert, M. Borgström, K. Deppert, K.A. Dick, J. Johansson, M.W. Larsson, T. Mårtensson, N. Sköld, C.P.T. Svensson, B.A. Wacaser, L.R. Wallenberg, and L. Samuelson, J. Cryst. Growth 272 (2004) 211.

[10] M. C. Plante and R. R. LaPierre, Journal of Crystal Growth 310 (2008) 356.

[11] M.C. Plante and R.R. LaPierre, Nanotechnology 19 (2008) 495603.

[12] P. Caroff, K.A. Dick, J. Johansson, M.E. Messing, K. Deppert, and L. Samuelson, Nat. Nanotech. 4 (2009) 50.

[13] Z. Ikonic, G.P. Srivastava and J.C. Inkson, Phys. Rev. B 48 (1993) 17181.

[14] J. Bao, D.C. Bell, F. Capasso, J.B. Wagner, T. Mårtensson, J. Trägårdh, and Lars Samuelson, Nano Lett. 8 (2008) 836.

[15] M.C. Plante and R.R. LaPierre, J. Appl. Phys. 105 (2009) 114304.

[16] C. Colombo, D. Spirkoska, M. Frimmer, G. Abstreiter, and A. F. I. Morral, Phys. Rev. B 77, 155326 (2008).

[17] H.J. Joyce, Q. Gao, H.H. Tan, C. Jagadish, Y. Kim, M.A. Fickenscher, S. Perera, T.B. Hoang, L.M. Smith, H.E. Jackson, J.M. Yarrison-Rice, X. Zhang, and J. Zou, Adv. Funct. Mater. 18 (2008) 3794.

[18] L. Geelhaar, C. Cheze, W. M. Weber, R. Averbeck, H. Riechert, T. Kehagias, P. Komninou, G. P. Dimitrakopulos, and T. Karakostas, Appl. Phys. Lett. 91, 093113 (2007).

[19] M. Jeppsson, K. A. Dick, J. B. Wagner, P. Caroff, K. Deppert, L. Samuelson, and L.-E. Wernersson, J. Cryst. Growth 310 (2008) 4115.

[20] T. Kitada, A. Wakejima, N. Tomita, S. Shimomura, A. Adachi, N. Sano, S. Hiyamizu, J. Cryst. Growth 150 (1995) 1.

[21] T. Sugaya, T. Nakagawa, Y. Sugiyama, Y. Tanuma, K. Yonei, Jpn. J. Appl. Phys. 36 (1997) 9A.

[22] Y. Kim, H.J. Joyce, Q. Gao, H.H. Tan, C. Jagadish, M. Paladugu, J. Zou, and A.A. Suvorova, Nano Lett. 6 (2006) 599.

[23] C. Chen, S. Shehata, C. Fradin, C. Couteau, G. Weihs, and R.R. LaPierre, Nano Lett. 7 (2007) 2584.

[24] P.K. Mohseni, A.D.Rodrigues, J.C.Galzerani, Y.A. Pusep, and R.R. LaPierre, J. Appl. Phys. (2009) in press.

[25] J. Johansson, L.S. Karlsson, K.A. Dick, J. Bolinsson, B.A. Wacaser, K. Deppert, and L. Samuelson, Cryst. Growth & Design 9 (2009) 766.

[26] J. Johansson, B.A. Wacaser, K.A. Dick, and W. Seifert, Nanotechnology 17 (2006) S355.

[27] J. Johansson, C.P.T. Svensson, T. Martensson, L. Samuelson, and W. Seifert, J. Phys. Chem. B 109 (2005) 13567.

[28] P. Krogstrup, J. Yamasaki, C.B. Sorenson, E. Johnson, J.B. Wagner, R. Pennington, M. Aagesen, N. Tanaka, and J. Nygard, Nano Lett. 9 (2009) 3689.

[29] T.B. Massalski, J.L. Murray, L.H. Bennet, H. Baker, Binary Alloy Phase Diagrams, American Society for Metals: Metals Park, OH, 1986, Vol. 1.

[30] K.A. Dick, K. Deppert, T. Martensson, S. Mandl, L. Samuelson, and W. Seifert, Nano Lett. 5 (2005) 761.

[31] F. Glas, J.C. Harmand, and G. Patriarche, Phys. Rev. Lett. 99 (2007) 146101.

[32] T. Akiyama, K. Nakamura, and T. Ito, Phys. Rev. B 73 (2006) 235308.

[33] T. Akiyama, K. Sano, K. Nakamura, and T. Ito, Jpn. J. Appl. Phys. 45 (2006) L275.

[34] V.G. Dubrovskii and N.V. Sibirev, Phys. Rev. B 77 (2008) 035414.

[35] V.G. Dubrovskii, N.V. Sibirev, J.C. Harmand, and F. Glas, Phys Rev. B 78 (2008) 235301.

[36] P.K. Mohseni and R.R. LaPierre, Nanotechnol. 20 (2009) 025610.

[37] K.A. Dick, P. Caroff, J. Bolinsson, M.E. Messing, J. Johansson, K. Deppert, L.R. Wallenberg, and L. Samuelson, Semicond. Sci. & Technol. 24 (2009) in press.

[38] S. Paiman, Q. Gao, H.H. Tan, C. Jagadish, K. Pemasiri, M. Montazeri, H.E. Jackson, L.M. Smith, J.M. Yarrison-Rice, X. Zhang, and J. Zou, Nanotech. 20 (2009) 225606.

[39] L.H.G. Tizei, T. Chiaramonte, D. Ugarte, and M.A. Cotta, Nanotech. 20 (2009) 275604.

[40] H. Shtrikman, R. Popovitz-Biro, A. Kretinin, L. Houben, M. Heiblum, M. Bukata, M. Galicka, R. Buczko, and P. Kacman, Nano Lett. 9 (2009) 1506.

[41] P. Caroff, K.A. Dick, J. Johansson, M.E. Messing, K. Deppert, and L. Samuelson, Nat. Nanotechnol. 4 (2009) 50.

Chapter 3

Modelling of InGaP Nanowire Morphology, Composition and Structure on Molecular Beam Epitaxy Growth Conditions

Many device applications require heterostructures containing III-V compound semiconductors such as InGaP for LEDs [4], GaAsP for near-infrared lasers [6] and quantum dot LEDs [8], InAsP for infrared photodetectors [5], and InGaAs for field-effect transistors [7]. Efforts have demonstrated the photovoltaic capabilities of III-V semiconductor NWs [1] where InGaP might be incorporated in a multi-junction design to improve energy conversion efficiency. Despite this, comparatively little work has been performed to understand the growth of ternary III-V compound semiconductor NWs as compared to elemental NWs such as Si, Ge and binary III-V NWs. We have previously reported on the influence of MBE growth conditions on morphology, composition, and crystal structure of InGaP NWs [20]. In this chapter we develop a detailed analytical model for the evolution of NWs depending on MBE growth parameters.

We first begin by discussing the physical model and the resulting model equations. We then provide a summary of the experimental data, identifying measurements that may be compared with model predictions. Thirdly, we provide details on our simulation approach and the physical significance of model parameters. We conclude this chapter with discussion of both the fit of the model to experimental data,

explaining the predictions of the model in terms of the impact of growth conditions, and discussing the observations that were driven by the model and simulations.

3.1 Model

Diffusion based models have successfully been applied to the case of binary nanowires [16]-[18]. In this work we extend these models to the case of ternary nanowires. We do this by taking into account the interaction between the different growth species, including the effect of composition on different model parameters, and making assumptions on equation boundary conditions to simplify the model equations. The resulting correspondence with experimental data and physical insights obtained from the model justify these simplifying assumptions.

Figure 3.1 shows the physical processes that contribute to the growth of nanowires in our system. Atomic or molecular species (In, Ga, P_2) impinge on the substrate surface from the vapor phase. For each species *i*, we denote the rate of impingement on the surface (atoms per unit area per unit time) by J_i. Atoms impinging on the Au seed dissolve and alloy with the Au and contribute to the nanowire growth. Atoms impinging onto the substrate surface adsorb as adatoms that diffuse along the 2D surface and then desorb from the surface, are captured by nucleation islands where they contribute to 2D

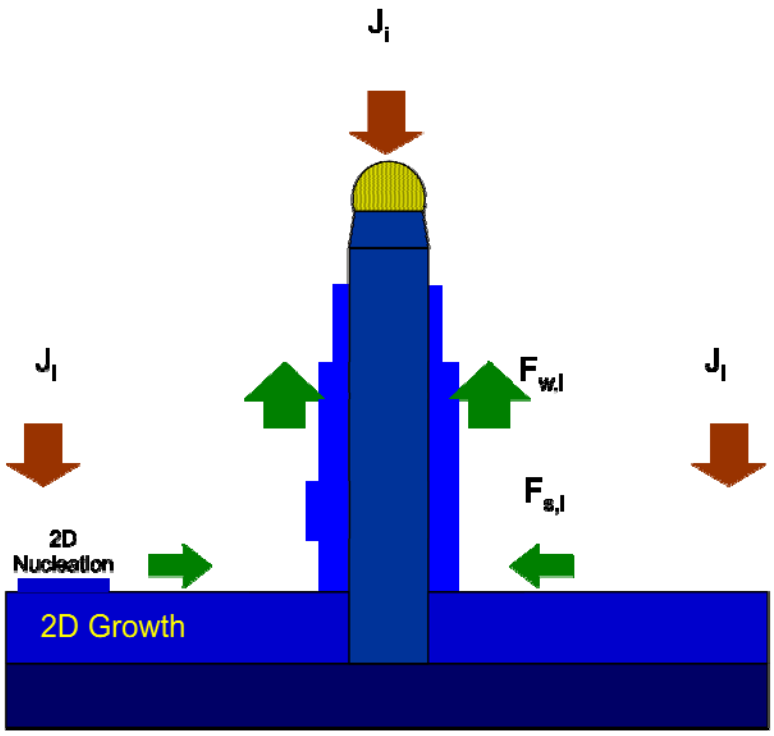

Figure 3.1 A Schematic of the diffusion based model.

surface growth, or arrive at the base of a nanowire. We denote the diffusion flux of species *i* on the surface by $F_{s,i}$. Atoms reaching the base of a nanowire diffuse upwards along the sidewalls of the wire until they either deposit on the sidewalls or reach the top of the wire. The flux of atoms of species *i* diffusing on the sidewalls of the wires we denote $F_{w,i}$. The flux of atoms reaching the top of the nanowire is denoted $F_{L,i}$; these adatoms dissolve in the liquid seed to contribute to the supersaturation of the Au droplet. These are therefore responsible for deposition from the Au seed at the top of the growing nanowire. Due to the relatively short lengths of the NWs and the substantial 2D film growth, the impingement on the NW sidewalls was ignored. In addition, our model strongly addresses the dependence of the growth on the interaction between the 2D island

nucleation and the onset of NW growth where the direct impingement on the sidewalls has minimal effect.

The surface diffusivity, $D_{s,i}$, of adatom *i* on the surface is a material property depending only on the diffusing species, the underlying surface material, and temperature. If we consider the "free" surface, without growth of new material, we may also characterize each adatom species with an average lifetime on the surface, $\tau_{0s,i}$, that describes the balance between adsorption, desorption and incorporation processes. We may also speak of a free surface diffusion length, $\lambda_{0s,i} = \sqrt{D_{s,i}\tau_{0s,i}}$. The parameters $\tau_{0s,i}$ and $\lambda_{0s,i}$ are also material properties. They are solely determined by the diffusing species, the stoichiometry and orientation of the underlying surface, and temperature. However, in a growth process where the surface is modified, nucleation islands, Au seeds, and nanowires act as sinks for the diffusing species. Under these circumstances, $D_{s,i}$ remains unchanged but the average lifetime and effective diffusion length will change. We will denote these variables as $\tau_{s,i}$ and $\lambda_{s,i}$ respectively, removing the subscript '0' that refers specifically to the free surface or "equilibrium" case. These parameters satisfy the relationship [28]

$$\frac{\lambda_{s,i}^2}{\tau_{s,i}} = \frac{\lambda_{0s,i}^2}{\tau_{0s,i}} = D_{s,i} \tag{3.1}$$

The effective diffusion length is determined by the free surface diffusion length and the density of sinks. In our case, possible sinks are the nanowires and nucleation islands. We may therefore write

$$\lambda_{s,i} = \frac{1}{\sqrt{\pi\left(N_w + N_I\right)}} \tag{3.2}$$

where N_I and N_w are the density of nucleating 2D islands and nanowire density, respectively. We will always have $\lambda_{s,i} \leq \lambda_{0s,i}$.

We assume that adsorption to and desorption from the surface, dissolution in and evaporation from the liquid, and incorporation in the solid phase are all much faster processes than the diffusion process. This means that the system will be in a quasi-steady state with the concentration of adatoms everywhere nearly constant in time, dependent only on the thermodynamic equilibrium between the different phases. Under this assumption, the appropriate equation describing the concentration of adatoms is the static diffusion equation [17],

$$D_{s,i}\nabla^2 n_{s,i} - \frac{n_{s,i}}{\tau_{s,i}} + J_i = 0 \tag{3.3}$$

where $n_{s,i}$ is the concentration of adatoms on the surface per unit area and depends on the growth conditions. It is useful to think of the free surface or equilibrium case and denote by $n_{0s,i}$ the equilibrium concentration of adatoms of species *i* on a surface of the given stoichiometry and orientation at the given temperature and pressure. This quantity is given by [19]

$$n_{0s,i} = \frac{1}{\sigma_{s,i}} \exp\left(-\frac{(2k_B T_C)}{k_B T} \right) \tag{3.4}$$

where $\sigma_{s,i}$ is the area per nucleation site for species *i*, the term $2k_B T_C$ is the phase-transition heat, where T_C is the critical temperature of the phase transition between rarefied and dense phases of the adsorbate, and *T* is the absolute temperature of the 2D

surface. Corresponding to this equilibrium concentration we may define an equilibrium impingement flux

$$J_{0,i} = \frac{n_{0s,i}}{\tau_{0s,i}} \tag{3.5}$$

Returning to Eq.(3.3) we may define the supersaturation of adatoms of species *i* as $\eta_{s,i} = \frac{n_{s,i}}{n_{0s,i}}$ and rewrite Eq. (3.3) in terms of the supersaturtion to get

$$D_{s,i}\tau_{s,i}\nabla^2\eta_{s,i} - \eta_{s,i} + \frac{J_i}{J_{0,i}}\frac{\tau_{s,i}}{\tau_{0s,i}} = 0 \tag{3.6}$$

which may be rewritten in terms of the effective diffusion length as

$$\lambda_{s,i}^2\nabla^2\eta_{s,i} - \eta_{s,i} + \frac{J_i}{J_{0,i}}\left(\frac{\lambda_s}{\lambda_{0s,i}}\right)^2 = 0 \tag{3.7}$$

For our model system we consider a single nanowire with material flowing to that wire from the surrounding area. We can do this because on average each wire is fed by adatoms impinging on a surrounding "collection area." The size of the collection area for a given wire is governed by the local density of Au seeds at the onset of growth. This has implications for the model parameters that we explore in more detail in subsequent sections.

Considering a single nanowire, Eq. (3.7) is reduced to a 1D equation with the supersaturation as a function only of radial distance from the center of the wire, $\eta_{s,i} = \eta_{s,i}(r)$. The solutions to the homogeneous part of Eq. (3.7) in 1D are the modified Bessel functions $\mathrm{I}_0\left(\frac{r}{\lambda_{s,i}}\right)$ and $\mathrm{K}_0\left(\frac{r}{\lambda_{s,i}}\right)$. However, for the homogenous case $J_i = 0$ and

we require solutions that tend to 0 as $r \to \infty$. This condition is only satisfied by $\mathrm{K}_0\left(\frac{r}{\lambda_{s,i}}\right)$. Therefore, the complete solution to Eq. (3.7) subject to this boundary condition is

$$\eta_{s,i}(r) = \frac{J_i}{J_{0i}}\left(\frac{\lambda_{s,i}}{\lambda_{0s,i}}\right)^2 + C_i \mathrm{K}_0\left(\frac{r}{\lambda_{s,i}}\right) \tag{3.8}$$

where C_i is a constant to be determined from a second boundary condition.

Wherever in the foregoing discussion we have used a subscript '*s*' to refer to the surface, we may define an analogous quantity on the wire sidewalls, for which we will use the subscript '*w*'. For example, $n_{w,i}, n_{0w,i}$, and $\eta_{w,i}$ will refer, respectively, to the concentration, equilibrium concentration, and supersaturation of adatoms of species *i* along the wire sidewalls.

The supersaturation of adatoms along the nanowire sidewalls will be a function only of distance from the base of the wire, $\eta_{w,i} = \eta_{w,i}(z)$ and has to satisfy the equation

$$\lambda_{w,i}^2 \frac{d^2\eta_{w,i}}{dz^2} - \eta_{w,i} = 0 \tag{3.9}$$

and the boundary condition $\eta_{w,i}(z \to \infty) = 0$, where $\lambda_{w,i}$ is the effective diffusion length along the wire sidewalls. This equation has a simple solution

$$\eta_{w,i}(z) = A_i \exp\left(-\frac{z}{\lambda_{w,i}}\right) \tag{3.10}$$

where A_i is a constant to be determined from a second boundary condition.

The boundary conditions required to determine A_i and C_i are that the supersaturation of adatoms and their flux be continuous at the base of the wire. This is a consequence of our assumption of a quasi-steady state and may be expressed as

$$\begin{aligned} &\eta_{w,i}(0) = \eta_{s,i}(R) \\ &n_{0w,i} D_{w,i} \left.\frac{d\eta_{w,i}}{dz}\right|_{z=0} = -n_{0s,i} D_{s,i} \left.\frac{d\eta_{s,i}}{dr}\right|_{r=R} \end{aligned} \tag{3.11}$$

where R is the radius of the wire during growth. This results in

$$\eta_{s,i}(r) = \frac{J_i}{J_{0i}} \left(\frac{\lambda_{s,i}}{\lambda_{0s,i}} \right)^2 \left\{ 1 - \frac{\mathrm{K}_0\left(\frac{r}{\lambda_{s,i}} \right)}{\mathrm{K}_0\left(\frac{R}{\lambda_{s,i}} \right) + \frac{n_{0s,i}}{n_{0w,i}} \frac{D_{s,i}}{D_{w,i}} \frac{\lambda_{w,i}}{\lambda_{s,i}} \mathrm{K}_1\left(\frac{R}{\lambda_{s,i}} \right)} \right\} \tag{3.12}$$

and

$$\eta_{w,i}(z) = \eta_{s,i}(R) \exp\left(-\frac{z}{\lambda_{w,i}} \right) \tag{3.13}$$

If we introduce the definition

$$\chi_i = \frac{n_{0s,i}}{n_{0w,i}} \frac{D_{s,i}}{D_{w,i}} \frac{\lambda_{w,i}}{\lambda_{s,i}} \tag{3.14}$$

we may rewrite Eq. (3.12) as

$$\eta_{s,i}(r) = \frac{J_i}{J_{0i}}\left(\frac{\lambda_{s,i}}{\lambda_{0s,i}}\right)^2 \left\{1 - \frac{\mathrm{K}_0\left(r/\lambda_{s,i}\right)}{\mathrm{K}_0\left(R/\lambda_{s,i}\right) + \chi_i \mathrm{K}_1\left(R/\lambda_{s,i}\right)}\right\} \tag{3.15}$$

The surface diffusion flux of species *i* arriving at the base of the wire is given by

$$F_{s,i} = -n_{0s,i} D_{s,i} \left.\frac{d\eta}{dr}\right|_{r=R} \tag{3.16}$$

Since this is a *surface diffusion* flux, it has dimension of atoms per unit time per unit length. Recalling that there is no angular variation we find the total dose of material arriving at the base of the nanowire in unit time by multiplying by the circumference at the base of the nanowire. Thus,

$$F_i = -2\pi R n_{0s,i} D_{s,i} \left.\frac{d\eta}{dr}\right|_{r=R} = -\frac{2\pi R \lambda_{s,i} J_i \mathrm{K_i}\left(R/\lambda_{s,i}\right)}{1 + \chi_i \mathrm{K_i}\left(R/\lambda_{s,i}\right)} \tag{3.17}$$

where we have introduced the definition

$$\mathrm{K_i}(r) = \frac{\mathrm{K}_1\left(r/\lambda_{s,i}\right)}{\mathrm{K}_0\left(R/\lambda_{s,i}\right)} \tag{3.18}$$

As discussed previously, and reflected in Eq.(3.13), some of the material arriving at the base of the wire gets deposited on the wire sidewalls so that we have

$$F_{w,i} = F_i \exp\left(-\frac{z}{\lambda_{w,i}}\right) \tag{3.19}$$

The amount of material arriving at the top of the wire to be introduced into the Au seed is given by

$$F_{L,i} = F_{w,i}\big|_{z=L} = F_i \exp\left(-\frac{L}{\lambda_{w,i}}\right) \tag{3.20}$$

Some of that material evaporates from the Au seed due to the Gibbs-Thompson effect. That dose is given by [17]

$$F_{GT,i} = \frac{x_i P_i^* \exp\left(\frac{2\gamma_l \Omega_l}{R k_B T}\right)}{\sqrt{2\pi m_i kT}} \tag{3.21}$$

where γ_l is the surface energy, Ω_l is the average molecular volume in the liquid, P_i^* is the vapor pressure of species *i* above its pure liquid, x_i is the mole fraction of species *i* in the InGaAu system, and m_i is the atomic mass of species *i*. The total amount of material deposited from the Au seed at the top of the wire will be given by $F_{L,i} - F_{GT,i}$ so that the wire growth rate will be given by

$$\frac{dL}{dt} = \sum_{III} \frac{\left(F_{L,i} - F_{GT,i}\right)\Omega_i}{\pi R^2} \tag{3.22}$$

where the sum is carried over the group III species since these are the growth limiting

species in our case. In Eq. (3.22) L is the wire length and Ω_i refers to the *molecular volume* of the III-V compound including species i.

3.2 Experimental Data

We have previously reported detailed experimental findings on the variation in the morphology and composition of InGaP nanowires grown under different experimental conditions [20]. Four samples of InGaP NWs were grown at several growth rates and V/III fluxes. Samples A, B, C and D were grown at a substrate temperature of 430 ℃, with growth rates of 2 μm/h, 1 μm/h, 0.25 μm/h and 0.25 μm/h , respectively. The V/III flux of the first three sample was set to 1.75 while sample D was grown with a V/III flux ratio of 8. These four samples were compared to a sample E grown with similar pressure conditions as sample B but at higher growth temperature of 510℃. These conditions are summarized in Table 3.1.

Samples A-D displayed similar elemental distribution dependence as a function of the nanowire length and width and the Au-seed diameter. Firstly, the In fraction was found to increase along the length of the nanowire, which indicates that In concentration increases relative to the Ga as the nanowires grow. Secondly, the nanowires acquired a core/shell structure, with the core being In-rich while the shell was Ga-rich. This was attributed to the higher diffusion length of In along the nanowire ($\lambda_{w,In}$) compared to that of Ga ($\lambda_{w,Ga}$). Thirdly, the In/Ga fraction in the core was found to decrease as the Au-seed diameter, d, or the growth rate decreased. Small diameter nanowires in sample C were simultaneously affected by both trends and as a result were GaP wires with no presence of In. Lastly, the In/Ga fraction was found to increase in sample D, despite having the same growth rate as sample C, when the V/III was increased from 1.75 to 8. Details are provided in Ref. [20].

Table 3.1 Growth conditions for samples used in this study.

Sample	Growth temperature (℃)	Group-III impingment flux (μm/h)	Growth Duration (Minutes)	V/III flux ratio
A	430	2	10	1.75
B	430	1	20	1.75
C	430	0.25	80	1.75
D	430	0.25	80	8
E	510	1	20	1.75

Although grown with the same rate and V/III ratio, the difference in growth temperatures between samples B (430℃) and E (510℃) had an impact on the elemental composition where nanowires of sample E were purely GaP with no trace of In along the nanowire, even though In was found in the Au-seed alloy. Furthermore, the density of nanowires in sample E was significantly lower compared to sample B, as shown in the scanning electron microscopy (SEM) images of

Figure 3.2. The figure shows very few grown NWs in sample E and Au particles distributed on the surface without any NW growth or minimal growth in the case of large Au diameters.

Therefore, for each of the samples A, B, C, D, the model should quantitatively predict the dependence of wire length on the Au seed diameter (L vs. d), the final observed NW width vs. the Au seed diameter (W/d vs. d), and the axial profile of the In/Ga ratio (In/Ga vs. L). In addition, the model should qualitatively explain the following phenomena:

a) Sample E grown at higher temperature exhibited a low density of NWs and no incorporation of In, compared with sample B;
b) Incorporation of In in sample D but not sample C (grown at lower V/III flux ratio) for small seed diameters, and higher In fraction for larger seed diameters;
c) For the same V/III flux ratio, decrease of In with decreasing growth rate; and
d) For a given sample, decrease of In with decreasing Au seed diameter.

Finally, to be physically consistent with the hypothesized phenomena, we expect $\lambda_{w,In} > \lambda_{w,Ga}$.

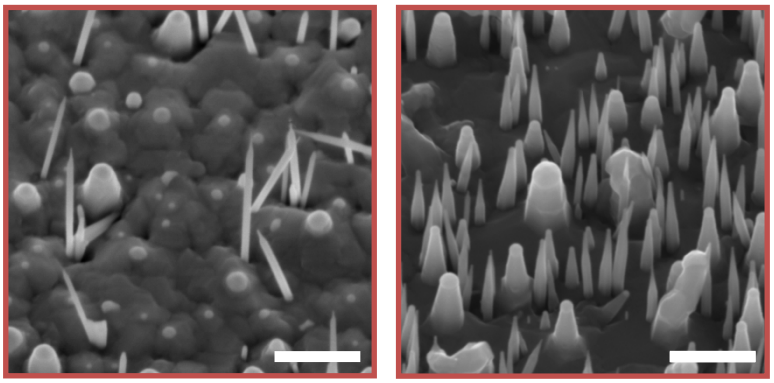

(a) **(b)**

Figure 3.2 SEM 30^{o} tilted view images for sample (a) E and (b) B. Scale bar indicates 500 nm.

3.3 Model Parameters and Simulation Approach

Eqs. (3.17)-(3.22) may be solved to predict all the properties of the nanowire. Eq. (3.22) yields the growth rate and final length of the nanowire. By discretizing the growth duration into n steps each of a duration Δt, the evolution of the nanowire length and width is discretized into n steps. The simulation starts with a primary step of 2 nm in length and an initial radius of R (see discussion below). The new segment forming with the new time step forms on the top of the previous one with diameter $2R$ and its length (dl_n) is calculated by Eq. (3.22). Figure 3.3 shows a schematic of the simulation process. At the end of the simulation, summation of dl for only the steps that are above the 2D surface produces the total length of the nanowire.

Eq. (3.22) also yields the fraction of In and Ga in the core region, the part of the nanowire grown directly under the Au seed, as a function of distance along the length of the nanowire. Similarly, Eq. (3.19) yields the fraction of In and Ga deposited on the sidewalls at a given height. A calculation similar to Eq. (3.22) gives the volume of material deposited on the sidewalls and therefore predicts the final tapering shape of the nanowire. The output of these equations and the simulation provide us with the core/shell structure, with In-rich core and Ga-rich shell, as shown in Figure 3.4.

We may now consider the parameters in the model equations, their physical significance, and their extraction from theory, measurement, or simulation.

The impingement rate, J_i, is a process parameter and must therefore be specified as an input to the model. The Ga and In impingement fluxes were equal for all of the samples. For Ga and In the fluxes in samples A, B, C, and D are, respectively, 5.324, 2.663, 0.666, and 0.666×10^{18} atoms/m^2·s. For P_2, the flux is obtained in each case by multiplying by half the V/III flux ratio.

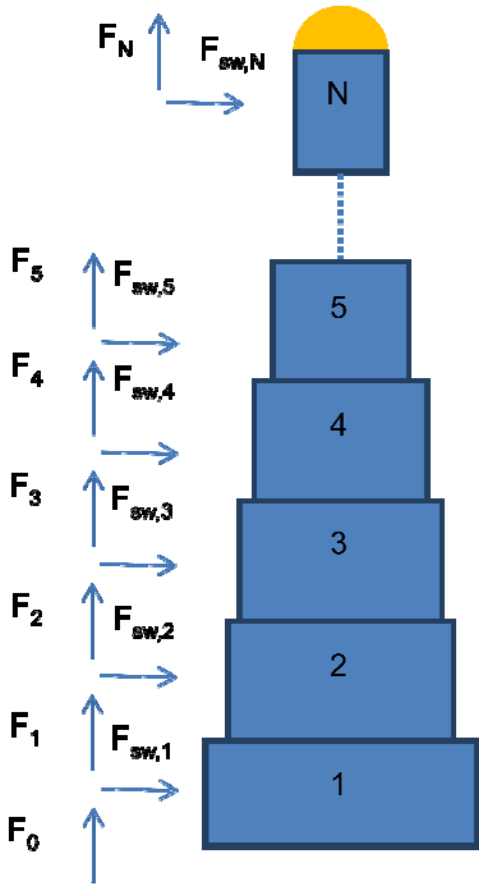

$$F_{sw,5} = F_0\left(e^{(-l_1'/\lambda_{nw})} - e^{(-l_5'/\lambda_{nw})}\right)$$

$$F_4 = F_0\left(e^{(-l_4'/\lambda_{nw})}\right)$$

$$F_{sw,4} = F_0\left(e^{(-l_3'/\lambda_{nw})} - e^{(-l_4'/\lambda_{nw})}\right)$$

$$F_3 = F_0\left(e^{(-l_3'/\lambda_{nw})}\right)$$

$$F_{sw,3} = F_0\left(e^{(-l_2'/\lambda_{nw})} - e^{(-l_3'/\lambda_{nw})}\right)$$

$$F_2 = F_0\left(e^{(-l_2'/\lambda_{nw})}\right)$$

$$F_{sw,2} = F_0\left(e^{(-l_1'/\lambda_{nw})} - e^{(-l_2'/\lambda_{nw})}\right)$$

$$F_1 = F_0\left(e^{(-l_1'/\lambda_{nw})}\right)$$

$$F_{sw,1} = F_0\left(1 - e^{(-l_1'/\lambda_{nw})}\right)$$

$$F_0 = F_{nw}(z = 0) = F_{diff}$$

Figure 3.3 Step-by-step growth of NW taking into account axial growth and sidewall deposition on each step.

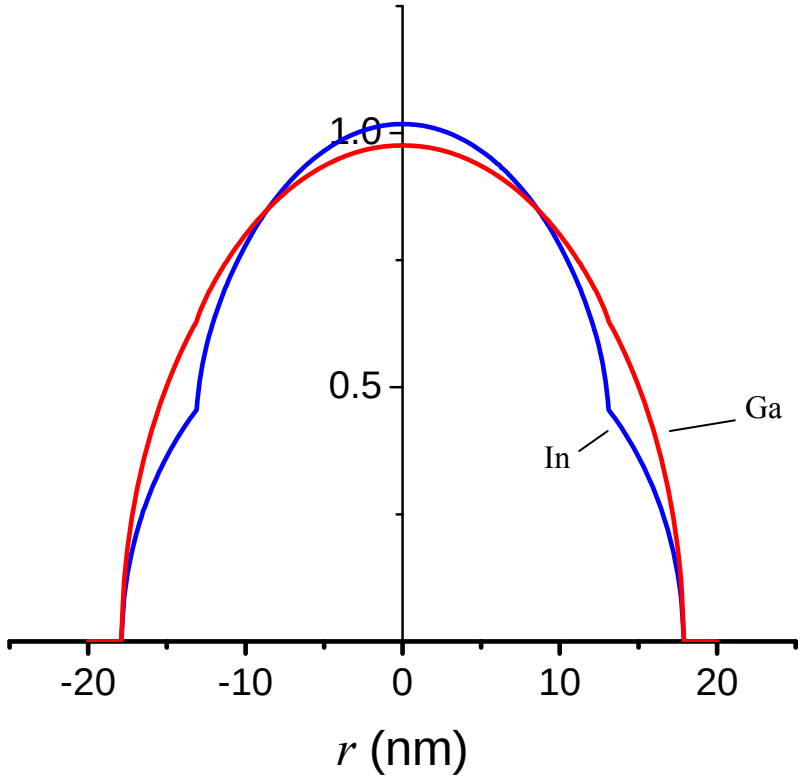

Figure 3.4 Elemental distribution along the NW radius of In (blue), Ga (red).

In Eq. (3.21), γ_l and Ω_l are obtained using Raoult's law [21], the m_i are known and values for P_i^* at 430°C were interpolated from the desorption curves for In and Ga using the Clausius-Clapeyron equation [17] and using heats of evaporation of 231.5 kJ/mol and 258.7 kJ/mol for In and Ga, respectively. The values we used are provided in Table 3.2.

Table 3.2 Material properties used in calculating the Gibbs-Thompson effect.

Parameter	In	Ga	Au
m	114.8	69.5	–
P^* at 430°C	6.28×10^{-8} Pa	1.07×10^{-10} Pa	–
γ_l	0.4886 N/m	0.683 N/m^2	1.272 N/m^2
Ω_l	2.61×10^{-29} m^3	1.91×10^{-29} m^3	1.89×10^{-29} m

The variables L, W and R describe the geometry of the wire. These are, respectively, the length of the nanowire, the final width of the base of the wire, and the radius of the Au-seed during growth. The first two are solution variables obtained from solving the equations at each time step. The last should ostensibly be the same as half the Au seed diameter, d, measured by transmission electron microscopy (TEM) post cool-down. However, due to the group-III purging from the Au seed alloy that takes place during cool-down after growth terminates, the diameter of the Au-seed particle during growth ($2R$) is different than the diameter, d, measured after cool-down [22]. Figure 3.5 shows a TEM image of a nanowire showing these two values. Seeds with small diameter ($\lesssim$ 20 nm), had a higher ratio of $2R/d$, and this ratio decreased as d increased. Compositional analysis done on the Au-seed particles using energy dispersive x-ray spectroscopy (EDX), showed that Au seed particles with diameters < 6 nm purge out all the In and Ga. As the diameter increased, the Ga fraction in the Au-seed particle increased, and for $d \geq 10$ nm, the In fraction in the Au-seed alloy increased. The purging out of the In and Ga from the Au seed for small diameters can be attributed to the GT effect, which, as shown in Eq. (3.21), is a function of the radius. Furthermore, the solubility of group-IIIs forming a eutectic alloy with Au differ in nano particles than that of bulk material [23], which could cause the purging of Ga and In for small diameter seeds to reach a stable state when the growth terminates and during the cool-down period. The exact relationship between $2R$ and d will depend on the

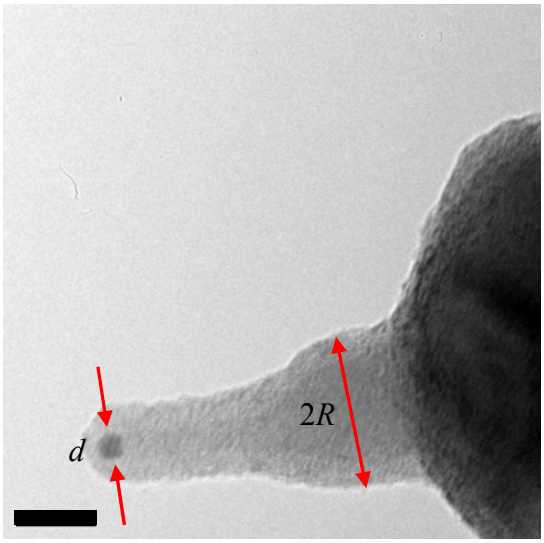

Figure 3.5 (a) TEM image of the top of a nanowire showing the difference between the diameter of the Au seed particle d and the diameter during growth $2R$. Scale bar indicates 10 nm.

characteristics of the cool-down period and the supersaturation of In and Ga during growth. From TEM micrographs both of these dimensions may be determined and so we have calibrated $2R$ as a function of d for each of the growth conditions used. Regardless of this correction, whether we assume $2R = d$ or we take into account the exact relationship between R and d, the model predicts different behavior depending on the size of the Au seed. In a given experiment the Au seed radius is a random variable following a particular distribution. Modeling the distribution of Au seed radius as a function of process conditions is beyond the scope of our work. Our model gives predictions as a function of the Au seed radius so that the morphology and composition of nanowires will follow a distribution corresponding to the distribution of Au seed radius.

The parameter χ_i plays a significant role in determining the diffusion fluxes of the different species. From Eq. (3.14) we see that this is a composite of three ratios. The ratio $\frac{\lambda_{w,i}}{\lambda_{s,i}}$ is fully discussed later in this chapter. The second ratio, $\frac{n_{0s,i}}{n_{0w,i}}$, may be calculated using Eq. (3.4). However, for a ternary system we must take into account the different composition on the nanowire sidewalls and the 2D surface. We therefore write $\frac{n_{0s,i}}{n_{0w,i}} = \frac{\sigma_{w,i}}{\sigma_{s,i}} \frac{0.5}{x_i}$, where x_i is the fraction of species i on the nanowire sidewall and the 2D surface is assumed to have approximately equal contributions of In and Ga. For our samples the facets of the nanowires are $\{\bar{2}110\}$ and a 2D surface of $\{111\}$, the ratio $\frac{\sigma_{w,i}}{\sigma_{s,i}} \approx 1.8$ so that we may write $\frac{n_{0s,i}}{n_{0w,i}} = 0.9 / x_i$. The mole fraction x_i thus appears in both Eq. (3.14) and Eq. (3.21). As the growth progresses, x_i is obtained as a solution variable from the model. However, the initial value of x_i is unknown and it is inaccurate to assume that it will be the same as the 2D surface. Rather, the initial value is the composition of an initial stump of material deposited under the Au seed. This initial value must satisfy

$$\frac{\pi R^2 J_{In} + F_{In}}{\pi R^2 J_{Ga} + F_{Ga}} = \frac{x_{In}}{x_{Ga}} \tag{3.23}$$

with $x_{In} + x_{Ga} = 1$. Therefore, we setup an initialization loop where we assume $x_{In} = 0.5$, solve the model equations, calculate a new x_{In} from the resulting fluxes and Eq. (3.23), and repeat until the loop converges to a self-consistent solution for x_{In}. We found that this loop converges rapidly (typically within about 10-13 iterations) and the resultant values of x_{In} are then compared to EDX measurements and used in the extraction of $\lambda_{s,i}$ and $\lambda_{w,i}$.

The ratio $\frac{D_{s,i}}{D_{w,i}}$ is a more complex matter. The surface diffusivity of an adsorbate on a given surface is given by the classic Arrhenius relationship $D = D_0 \exp^{-Q_{diff}/kT}$. Reference [27] attempts to give a full survey of available values as well as some approaches to calculating the effect of different factors such as composition, crystal structure, and orientation. In the low temperature regime (below about $0.5T_m$) surface diffusion on a semiconductor surface is widely accepted to be by site-to-site hopping and not a correlated process involving defects such as vacancies or concerted exchange of multiple atoms. Under these circumstances the prefactor D_0 is expected to be very nearly 1×10^{-7} cm^2/s and would not be significantly affected by stoichiometry, crystal structure, or orientation. The energy Q_{diff} is expected to be comprised of two components: ΔH_f, the energy of formation of the adatom, and ΔH_m, the energy of migration. The latter quantity should be proportional to the desorption energy, Q_{des}. Thus, any difference between the surface diffusivity on the nanowire sidewall and the 2D surface has to be attributed to changes in either ΔH_f or Q_{des}. The change in the energy of formation in GaP and InP from the wurtzite to the zincblende structures are well documented and are given by, respectively, 18.3 meV and 6.8 meV [28]. Considering that the change in formation of an adatom on the surface is a fraction ($\frac{2}{3} - \frac{2}{9}$, depending on the type of material and the temperature regime) the difference due to formation of adatoms is seen to be negligible. For the energy of migration we may write $\Delta H_m = \Omega Q_{des}$ where Ω is known as the corrugation ratio. Reference [27] cites both experimental and theoretical evidence that Ω decreases with an increase in the number of covalent bonds that the adatom makes with the surface. However, we observe that as the number of bonds increases Q_{des} also increases so that there is a net increase in ΔH_m. The point of these remarks is that the increase in ΔH_m between the nanowire sidewalls and the 2D surface due to crystallographic orientation and crystal structure are expected to be a very small fraction of Q_{des}, probably on the order of about 10%. Noting further that the $Q_{des} = 2.32\text{eV}$ for Ga

on GaP and 1.06eV for In on InP, where these values were extracted from the equilibrium pressure Arrhenius plots of Ga on GaP and In on InP, respectively, we may conclude that ΔH_m from all sources will be in the range of about 0.1 – 0.25 eV. Reference [25], considering the growth of GaAs nanowires on GaAs substrates, used a value of 0.1, citing Reference [27]. Unfortunately it is not clear how a specific value could be obtained either from the experimental data or theoretical arguments given in [27]. Reference [24] uses a value close to 0.01 but does not cite a source for the numbers used. Based on the qualitative arguments we have given here, at our growth temperature of 430°C, we expect $\frac{D_{s,i}}{D_{w,i}}$ to be in the range 0.025 – 0.2. We expect this number to be a constant across all our samples. We found that a value of 0.1 fits our data well. Any variation in this number would require re-optimization of the actual fitting parameters in our model, i.e. the effective diffusion lengths discussed below. With that caveat, variations in $\frac{D_{s,i}}{D_{w,i}}$ within the range calculated here will not have a dramatic effect on the simulations.

The fitting parameters that remain are $\lambda_{s,i}$ and $\lambda_{w,i}$. We used these as fitting parameters to predict L, W (final width at the base of the nanowire), F_i, and $x_i(r,z)$ for our samples, all as functions of the Au seed diameter, d. Figure 3.6 shows the results of samples A-D. Figure 3.6 (a, d, g, j) shows the variation of wire length with Au seed radius (L vs. d) for samples A-D, respectively. Figure 3.6 (b, e, h, k) and (c, f, i, l) for samples A-D, respectively, show the variation of the final wire base width with the Au seed parameter (W/d vs d), and the In/Ga fraction along the nanowire length, respectively. The discontinuity in the fitting curve in Figure 3.6 (g) represents the onset of In presence in the NWs, where NWs of small diameter of sample C are In-free and In starts to contribute in the NW growth for larger diameter values. The experimental data for In fraction along the length of the wire was obtained by TEM-EDX measurements, which become noisier as we get nearer to the tip of the wire due to the narrowing of the wire and the damage

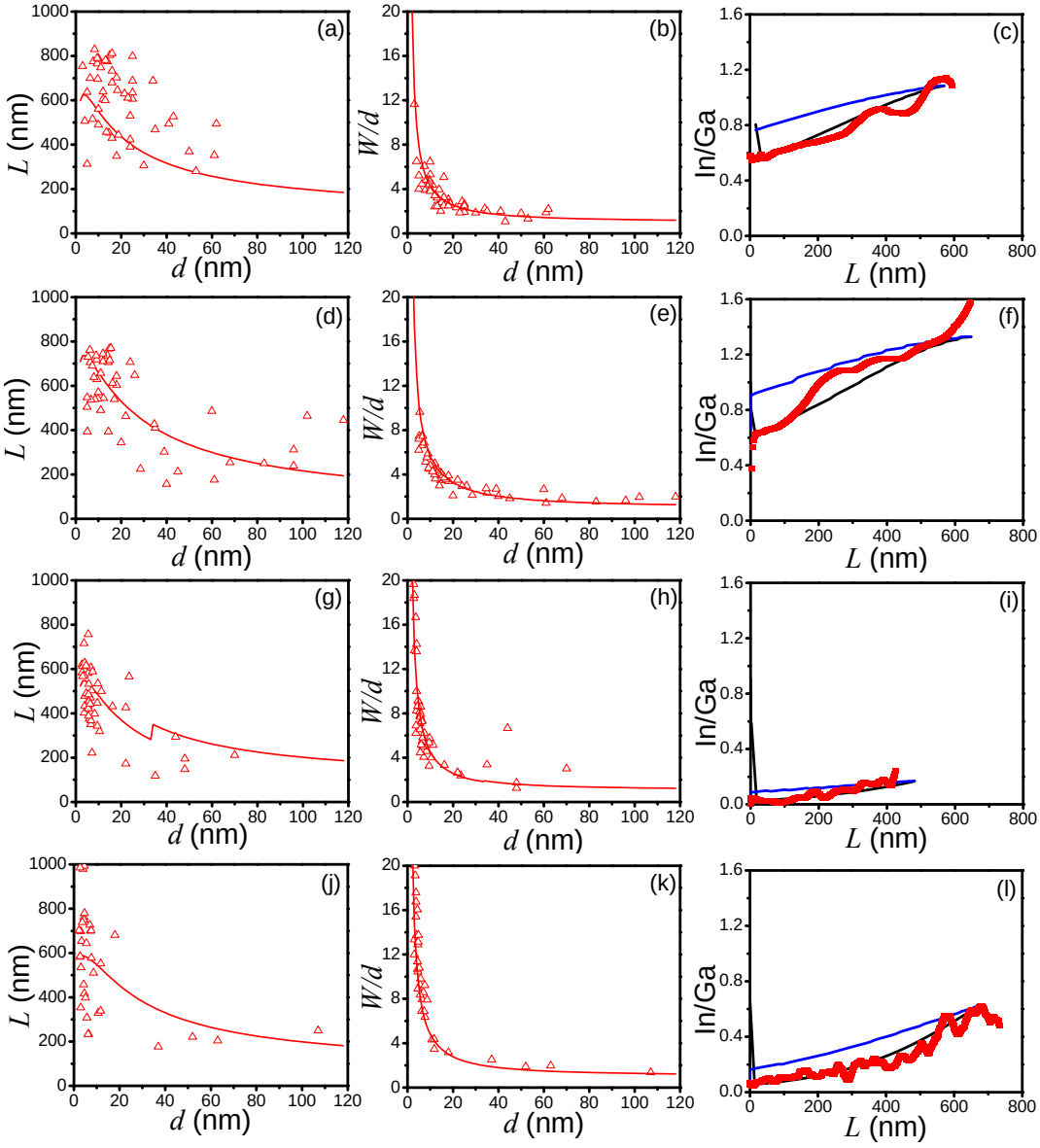

Figure 3.6 Experimental data (data points) and simulation results (solid lines) showing (a, d, g, j) *L* vs *d*, (b, e, h, k) *W*/*d* vs *d* and (c, f, i, l) The ratio of In/Ga as obtained from EDX measurements (black line) and the corresponding core composition of In/Ga from the simulation (black line), for samples A, B, C and D, respectively.

over the course of the measurement. We have therefore used a moving average to smooth the data. We produce other data in the next section when we discuss the physical insights arising from these simulations.

The values of $\lambda_{w,i}$ obtained for our various samples are given in Table 3.3. The values of $\lambda_{s,i}$ are expected to vary with d because narrower wires will tend to have associated with them smaller collection areas and greater local nanowire density, N_w. Figure 3.8 shows the obtained $\lambda_{s,i}$ as a function of d for each of our samples. This dependence is discussed further in the next section.

To recap, the only true fitting parameters in this model are the $\lambda_{s,i}$ and $\lambda_{w,i}$. We have extracted values for these two parameters that result in excellent fits to all our data. In the next section we discuss in detail the physical justification for these values. All other parameters in the model are either inputs to it or calculated from first principles as discussed previously.

Table 3.3 Values of $\lambda_{w,i}$ for the grown samples

Sample	$\lambda_{w,Ga}$ (nm)	$\lambda_{w,In}$ (nm)
A	180	240
B	180	240
C	180	600
D	180	400

3.4 Discussion

Wire growth, nanowire density, and indium inclusion

In the system there is interaction between four phases: vapor (*V*), adsorbed atoms (*A*), the Au seed liquid phase (*L*), and the solid (*S*). There is 2D surface growth with a nucleation island density N_I, growth from the Au seed into the core of the nanowire, and growth on the sidewalls of the wire. The density of the nanowires is N_W and corresponds to the density of Au seeds on the surface at the onset of nanowire growth.

Using the solid phase as a reference, the chemical potential of a given atomic species, *i*, in a given phase, *X*, may be expressed as:

$$\Delta\mu_{XS,i} = kT \ln \phi_{XS,i} \tag{3.24}$$

where $\phi_{XS,i}$ is the supersaturation of species *i* in phase *X*.

For the vapor phase,

$$\phi_{VS,i} = \frac{J_i}{J_{0i}} \tag{3.25}$$

where J_{0i} can be extracted from the equilibrium vapor pressure curves , P_{0i}, available in the literature. The relation between J_{0i} and P_{0i} is governed by the Langmuir's evaporation equation.

For the adatom phase the supersaturation away from any wire or nucleation site was obtained from Eq. (3.12),

$$\phi_{AS,i} = \frac{J_i}{J_{0i}} \left(\frac{\lambda_s}{\lambda_{0s}} \right)^2 \tag{3.26}$$

For the Au seed,

$$\phi_{LS,i} = \frac{n_{w,i}(L)}{C^*_{Au,i} V_{Au}} \tag{3.27}$$

where $C^*_{Au,i}$ is the equilibrium solubility of species *i* in the Au seed and V_{Au} is the volume of the Au seed. Although we do not intend to use Eq. (3.27) for quantitative computations in this work, it should be noted that the solubility $C^*_{Au,i}$ is not only a function of temperature and pressure; it will also be a function of the concentrations of the different species in the Au seed. (This equation is also inaccurate in that it ignores the contribution to the supersaturation of atoms in the Au seed arising from direct impingement onto the Au seed.)

The thermodynamic condition for 2D surface growth or sidewall nanowire growth involving species *i* is $\phi_{VS,i} > \phi_{AS,i} > 1$. The condition for nanowire growth involving species *i* from the Au seed is

$$\phi_{VS,i} > \phi_{AS,i} > \phi_{LS,i} > 1 \tag{3.28}$$

In ternary systems such as InGaP, the enthalpy of mixing during nucleation is minimized by nucleation taking the form of separate GaP and InP nuclei and hence we assume the presence of two separate systems, InP and GaP. Model equations treat In and Ga separately, while the joint factor between the two systems, J_{P2}, will be split between the two. Consequently, there will be four species, *i*, in our equations: In, Ga, P_2(InP) for the portion of P_2 needed for InP nucleation, and P_2(GaP) for the portion of P_2 responsible for GaP nucleation.

To analyze the two systems, the best point to start is from the vapor phase of the impinging atoms. Equilibrium vapor pressure curves, P_{0i}, are available in the literature for InP and GaP which by applying Langmuir's evaporation equation, these curves can be plotted in terms of equilibrium vapor fluxes J_{0i}, for InP and GaP, separately. These fluxes are described in the form of J_{0In} and J_{0P_2} over InP for InP system and J_{0Ga} and J_{0P_2} over GaP for the GaP system. However, in our analysis, we deal with a ternary system and would need to describe the equilibrium vapor pressures J_{0In}, J_{0Ga} and J_{0P_2} to be over InGaP rather that InP or GaP only.

The fluxes J_{0i} represent an equilibrium between adsorption and desorption involving $n_{0,i}$ desorption sites for species *i*. On the ternary InGaP surface the desorption sites allocable to each of our two model systems should be proportional to the fraction of In/Ga in the 2D surface and inversely proportional to the lifetime of each species would also be expected to change. As an approximation, we will ignore the change in $\tau_{0,i}$ and will consider the $n_{0,i}$ to be halved. Hence, Eq. (3.25) should be modified to

$$\phi_{VS,i} = \frac{J_i}{J_{0i}} = \frac{J_i}{\frac{\left(P_{0i}/2\right)}{\sqrt{2\pi m_i k_B T}}} \tag{3.29}$$

where the factor 1/2 factor in the denominator represents the transformation of the desorption flux curves from J_{0In} and J_{0P_2} over InP for InP system and J_{0Ga} and J_{0P_2} over GaP for the GaP to J_{0In}, J_{0Ga} and $J_{0P_2,InP}$ $J_{0P_2,GaP}$ to be over InGaP. The resultant equilibrium desorption flux curves for J_{0i}, for all values of *i*, is shown in

Figure 3.7 (a) and the corresponding values of $\phi_{VS,i}$, as calculated from Eq.(3.29), are plotted in Figure 3.7 (b).

Conceptually we may think of an initial equilibrium between adsorbed atoms and the vapor phase with $\lambda_{s,i} = \lambda_{0s,i}$. Since $\phi_{AS,i} > 1$, 2D surface growth proceeds and the surface densities N_I and N_w starts to show their effect on $\lambda_{s,i}$, as described by begins Eq. (3.2), where $\lambda_{s,i}$ decreases. Ultimately, the effect is conveyed to $\phi_{AS,i}$ and it decreases. While we have expressed this mathematically as a result of the decrease in the effective diffusion length, physically this represents the depletion of adsorbed atoms due to nucleation and island growth so that the supersaturation of adsorbed atoms on the surface is less than the vapor phase. Typically, values of $\left(\lambda_{s,i}/\lambda_{0s,i}\right) \approx 0.01 - 0.1$.

Simultaneously, the Au seed acts as a sink for the adsorbed atoms, which then diffuse towards the Au seed thus increasing the supersaturation in the Au seed. The onset of nanowire growth is inherently a dynamic process requiring sufficient time to establish the thermodynamic condition Eq. (3.28) for the growth species. Depending on the growth conditions this may be achieved for either InP, GaP, both, or neither. Figure 3.7 (b) shows the resulting $\phi_{VS,i}$ for the four species as a function of temperature for samples B, C, and E in our experiments. The values of $\phi_{VS,Ga}$ is much greater than the others, which establishes that the supersaturation of Ga is much higher than the other species and it is not a limiting factor in the growth. Hence, we excluded it from the plot. Similar to $\phi_{VS,Ga}$, $\phi_{VS,P_2(GaP)}$ does not seem to be a limiting factor in the growth of the GaP due to its high value. For the other two growth species that are responsible for the growth of InP, the values for their supersaturation seem to be much smaller. The impact of this low supersaturation becomes important when $\phi_{AS,In}$ and $\phi_{AS,P_2(InP)}$ are calculated, as shown in Figure 3.7 (c) for sample C. The value of $\phi_{AS,P_2(InP)}$, in particular, becomes very close to unity and nullifies the driving force for the nucleation of InP in the nanowire, producing a pure GaP nanowire. However, when the V/III ratio is increased in sample D, the

$\phi_{AS,P_2(InP)}$ becomes greater than $\phi_{AS,In}$ and produces enough supersaturation for InP nucleation and makes the $\phi_{AS,In}$ to be the critically limiting supersaturation for InP growth.

The values of $\phi_{AS,In}$ and $\phi_{AS,P_2(InP)}$ for sample B and E can assist us in explaining three observations. First, the absence of In in nanowires in sample E is justified by the fact that either $\phi_{AS,In}$ and $\phi_{AS,P_2(InP)}$ or both are less than unity. Therefore, the nanowires in this sample will be pure GaP as experimentally observed. Additionally, the nanowire density in this sample was lower than in sample B. This is the second phenomenon explained by the foregoing discussion since $\phi_{VS,Ga}$ for sample E is less than that in sample B implying that it will require a longer time to establish the thermodynamic condition Eq. (3.28), during which time the Au seeds continue to migrate on the surface and coalesce into larger, fewer seeds. This also explains the third observation that the average Au seed diameter is larger for sample E than sample B.

Au seed size effects

We have already discussed the fact that at the end of the growth, there is a cool down purge during which In and Ga evaporate from the seed as it cools down, resulting in a shrinkage of the Au seed to its final diameter, *d*. We have also noted that the shrinkage can be quite significant for small size seeds. Considering this in reverse, this indicates that the inclusion of Ga and In results in significant expansion of the Au seed initially. For small Au seed diameters we would expect the low supersaturation of In adatoms to preclude the inclusion of In in the seed. We would expect wires under these Au seeds to be pure GaP. However, once Ga is incorporated in a seed, its volume expands resulting in

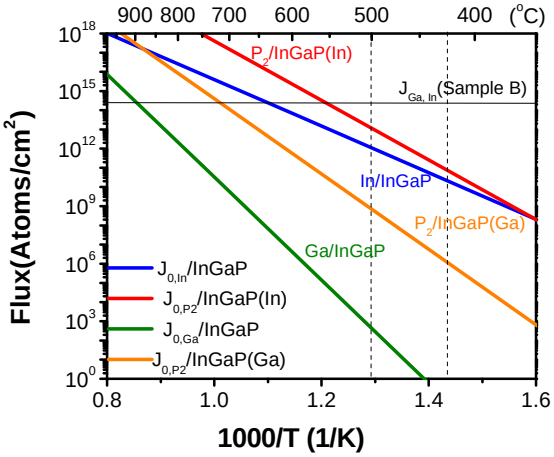

(a)

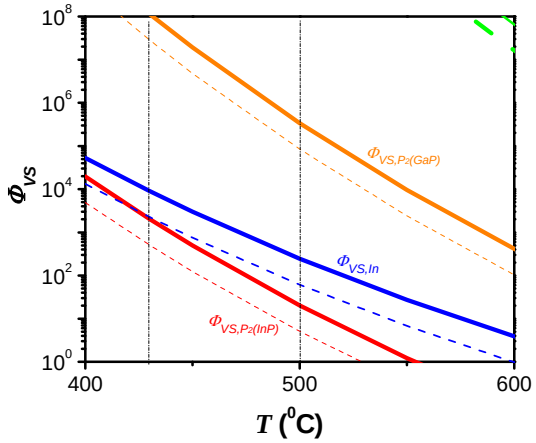

(b)

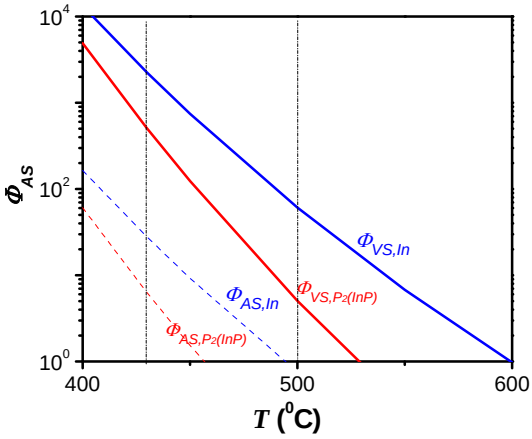

(c)

Figure 3.7 (a) The equilibrium flux J_0 vs. $1000/T$ on the bottom axis and T(℃) on the top axis, (b) Φ_{VS} versus T(℃) for samples B,E (1μm/hr) (solid line) and C (0.25μm/hr)(dashed line) and (c) Φ_{VS} (solid line) and Φ_{AS} (dashed line) for sample C (0.25μm/hr).

a lower GT effect so that more In may be incorporated in the seeds. At the end of the growth, both Ga and In are purged from the seed returning it to its original (small) size. Therefore, in the presence of Ga it is possible to grow InGaP nanowires under Au seeds down to 1.5-2 nm in radius as we have observed in our own samples. This is in stark contrast to experiments where pure InP nanowires have been grown, where the smallest seeds resulting in nanowire growth are close to 12 nm in radius, with cut-off GT radius ~ 4 nm [21].

Effective diffusion length on the 2D surface

We are finally in a position to give a detailed discussion of the four diffusion lengths that comprise the true fitting parameters in our model. The value of the effective diffusion length on the 2D surface is given by Eq.(3.2).

$$\lambda_{s,Ga} = \lambda_{s,In} = \frac{1}{\sqrt{N_w + A}} \tag{3.30}$$

where A was the remaining fitting parameter that varied from one sample to another. The value of N_w were determined from measurement and it was found to vary among the sample. It has been observed that N_w is large for nanowires with small diameters and becomes smaller for nanowires with larger diameters. This is expected due to the coalescence of small Au particles to form larger ones. Thus, the sum of the areas of the small particles become the area of the larger formed Au seed. To model this effect we used a linear sweep to describe N_w versus d.

The resulting behavior is shown in Figure 3.8. As expected, the value of λ_s is a nearly linear function of d, and it increases with decreasing ϕ_{VS}.

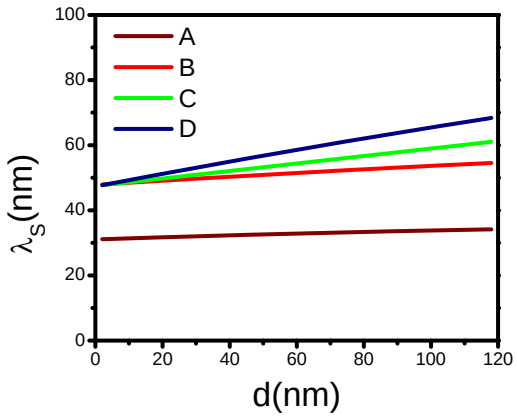

Figure 3.8 The values of λ_S vs the diameter of the seed particle.

Table 3.3 shows the values of $\lambda_{w,Ga}$ and $\lambda_{w,In}$ for each of our four samples, where $\lambda_{w,In} > \lambda_{w,Ga}$ for all samples. As expected, these diffusion lengths also increase with decreasing ϕ_{VS}. However, this effect is not dominant on $\lambda_{w,Ga}$ and this can be attributed to the extremely high values of $\phi_{VS,Ga}$ which would cause any fluctuations in its value to be insignificant compared to the great driving from sustained by its absolute value.

3.5 Conclusion

We have successfully modeled the growth of InGaP nanowires using Au assisted MBE growth. Our model requires as input only the fluxes of the different species and the diameter of the Au seed. Because each sample contains a distribution of Au seed diameters, measured wire properties will also display a distribution. Because of purge during cool-down, the Au seed diameter during growth is different from the diameter

measured after the cool-down. This difference is more significant for seed radii below about 10 nm. The relationship may be calibrated by noting the radius of the "neck" of the nanowire from TEM measurements. We used that to calibrate the Au seed radius during growth to use as input in the model equations. We considered the effective surface diffusion length on the 2D surface to be equal for In and Ga and considered it to be an increasing function of nanowire radius and a decreasing function of the chemical potential difference between the vapor and 2D surface. We took the surface diffusion lengths along the nanowire sidewalls as fitting parameters and found, as expected, that $\lambda_{w,In} > \lambda_{w,Ga}$. Our model explains the increasing incorporation of In along the length of the wire, the core-shell structure of the wires, and predicts the dependence of wire morphology and composition on process conditions and Au seed diameter. We found that increasing the group III flux or the V/III flux ratio resulted in denser, longer wires with higher incorporation of In.

References

[1] J. A. Czaban, D. A. Thompson, and R. R. LaPierre, Nano Letters **9**, 148 (2009).

[2] T. Stelzner, M. Pietsch, G. Andra, F. Falk, E. Ose, and S. Christiansen, Nanotechnology **19** (2008).

[3] O. Gunawan and S. Guha, Solar Energy Materials and Solar Cells **93**, 1388 (2009).

[4] C. Svensson, T. Martensson, J. Tragardh, C. Larsson, M. Rask, D. Hessman, et al., Nanotechnology **19**, 305201 (2008).

[5] H. Pettersson, J. Tragardh, A. I. Persson, L. Landin, D. Hessman, and L. Samuelson, Nano Letters **6**, 229 (2006).

[6] Hua **B**, Motohisa J, Kobayashi Y, Hara S and Fukui T, Nano Letters **9**, 112 (2009).

[7] Noborisaka J, Sata T, Motohisa J, Hara S, Tomioka K and Fukui T, Japan J. Appl. Phys. **46**, 7562 (2007).

[8] Minot E D, Kelkensberg F, Kouwen M v, Dam J A v, Kouwenhoven L P, Zwiller V, Borgstrom M T, Wunnicke O, Verheijen M A and Bakkers E P A M, Nano Letters **7**, 367 (2007).

[9] F. Qian, S. Gradecak, Y. Li, C.-Y. Wen, C.M. Lieber, Core/multishell nanowire heterostructures as multicolor, high-efficiency light-emitting diodes, Nano Letters **5**, 2287 (2005).

[10] F. Patolsky, G. Zheng, C. Lieber, Anal. Chem. **78**, 4260(2006).

[11] Y. Li, J. Xiang, F. Qian, S. Gradecak, Y. Wu, H. Yan, et al., Nano Letters **6**, 1468(2006).

[12] R. S. Wagner and W. C. Ellis, Applied Physics Letters **4**, 89 (1964).

[13] K. Hiruma, T. Katsuyama, K. Ogawa, M. Koguchi, H. Kakibayashi, G.P. Morgan, Appl. Phys. Lett. **59**, 431 (1991).

[14] M. C. Plante and R. R. LaPierre, Journal of Crystal Growth **286**, 394 (2006).

[15] L. E. Jensen, M. T. Bjork, S. Jeppesen, A. I. Persson, B. J. Ohlsson, and L. Samuelson, Nano Lett. **4**, 1961 (2004).

[16] V. G. Dubrovskii, G. E. Cirlin, I. P. Soshnikov, A. A. Tonkikh, N. V. Sibirev, B. S. Yu, and V. M. Ustinov, Physical Review B (Condensed Matter and Materials Physics) **71**, 205325 (2005).

[17] J. Johansson, C. P. T. Svensson, T. Martensson, et al., The Journal of Physical Chemistry B 109, 13567 (2005).

[18] M. C. Plante and R. R. LaPierre, Journal of Applied Physics **105** (2009).

[19] V. G. Dubrovskii, Journal of Physics: Condensed Matter **16**, 6929 (2004).

[20] A. Fakhr, Y. M. Haddara and R. R. LaPierre,., Nanotechnology **21**, 165601 (2010).

[21] V. G. Dubrovskii, et al., Physical Review B (Condensed Matter and Materials Physics) **79**, 205316 (2009).

[22] M. C. Plante and R. R. LaPierre, Nanotechnology, 495603 (2008).

[23] N. Braidy, G. R. Purdy, and G. A. Botton, Acta Materialia **56**, 5972 (2008).

[24] V. Dubrovskiĭ, N. Sibirev, G. Cirlin, and V. Ustinov, Semiconductors **40**, 249 (2006).

[25] N. Sibirev, V. Dubrovskii, E. Arshanskii, G. Cirlin, Y. Samsonenko, and V. Ustinov, Technical Physics **54**, 586 (2009).

[26] V. G. Dubrovskii and N. V. Sibirev, Journal of Crystal Growth **304**, 504 (2007).

[27] *Landolt-Bornsstein Group III Condensed Matter* (Springer, Berlin, 2006), Vol. 41 A1a.

[28] V. G. Dubrovskii, N. V. Sibirev, J. C. Harmand, and F. Glas, Physical Review B (Condensed Matter and Materials Physics) **78**, 235301 (2008).

Chapter 4

Growth Rate Dependence of MBE-Grown InGaP Nanowire Crystal Structure

Semiconductor NWs are being explored for a variety of applications [1]-[3]. Unlike bulk III-V semiconductors that exists in the ZB phase, III-V NWs are mostly WZ in structure with random ZB insertions along its axis. These defects along the axis can change the optical and electronic properties of the NWs and, hence, controlling the phase of the NW [5] and eliminating the defects to provide perfect phase NWs is important[6].

The WZ phase of NWs has been explained by several theoretical models. Early models attributed the occurrence of WZ in NWs due to the lower surface energy of WZ when compared to ZB at small NW diameters [7]-[8]. This model estimated that NWs would turn from the WZ to ZB phase for NW diameters exceeding a certain calculated critical diameter. However, the estimated diameter that differentiated WZ and ZB formation was underestimated, as NWs reported in literature with much larger diameter than the critical diameter were WZ. The nucleation-based model, established by Glas et. al [9], showed that nucleation at the seed-NW interface takes place at the triple-phase-line (TPL). Nucleation at the TPL energetically favors the WZ phase at high super-saturation

of the group-III element in the Au-III alloy, whereas the ZB phase was favored at low super-saturation. The estimation of the resultant crystal structure of the NW was determined by treating each nucleating event as a random Poisson process [10]. Several modifications and additions to this approach has followed to improve the understanding of the phase changes. In [11], the NW formation and crystal structure was described taking the Gibbs-Thompson effect (GT) into account. Phase transition dependence on diameter was discussed [12] and attributed to the change in the GT effect. The growth study of several NW facet orientations and the surface energies of the growth interface and the nucleus were studied in [6] to produce perfect phase NWs. More recently, combinational approaches have been utilized to understand the occurrence of other unusual higher order polytypes (4H and 6H) that can result in NWs [13].

Experimental results of InGaP NWs grown using molecular beam epitaxy were previously discussed [14]. In this chapter, we explain the crystal structure behaviour using the nucleation-based model combined with the kinetic growth model. The key in our approach is to differentiate between the growth species in the growth kinetic model and the nucleation-based model, and deal with each species separately. Finally, we conclude based on our results and model, that each growth species enforces different phase formation.

4.1 Model

In the nucleation-based model, the TPL is the energetically favored location for the nucleation of a new monolayer, as shown in Figure 4.1. A competition between WZ and ZB nucleation takes place and the value of the nucleation barrier for the formation of its critical nucleus for each crystal phase play the major role in its formation. The crystal phase that has the lower nucleation barrier becomes the energetically favorable phase to

form. The process of a specific phase to nucleate is described by the probability of this phase to form using a random Poisson process to describe it [10]:

$$P_\phi = \frac{e^{-\Delta G_\phi^* / k_B T}}{\sum_\phi e^{-\Delta G_\phi^* / k_B T}}, \tag{4.1}$$

where ΔG_ϕ^* is the nucleation barrier of the critical nucleus for a certain phase ϕ, which refers to the phases WZ or ZB, k_B is Boltzmann constant and T is the absolute temperature.

In a ternary system like InGaP, the energy of formation for a new nucleus is minimized by having InP and GaP nucleate separately. This case has been discussed for the case of ternary InGaP NWs, as discussed in the previous chapter, and two flux components, F_{In} and F_{Ga}, contributing to the growth has been derived for InP and GaP, respectively. As the growth fluxes reach the Au droplet and undergo the nucleation process, InP and GaP are expected to nucleate separately. In addition, each of the InP and the GaP is subjected to the random Poisson nucleation process separately, which results in the probability of phase formation to be:

$$P_\phi = \bar{F}_{In} \cdot \frac{e^{-\Delta G_{In,\phi}^* / k_B T}}{\sum_\phi e^{-\Delta G_{In,\phi}^* / k_B T}} + \bar{F}_{Ga} \cdot \frac{e^{-\Delta G_{Ga,\phi}^* / k_B T}}{\sum_\phi e^{-\Delta G_{Ga,\phi}^* / k_B T}}, \tag{4.2}$$

where $\bar{F}_{In} = F_{In} / \left(F_{In} + F_{Ga} \right)$ and $\bar{F}_{Ga} = F_{Ga} / \left(F_{In} + F_{Ga} \right)$.

Derivation of the nucleation barriers ΔG_ϕ^*, for the InP and GaP is essential to calculate the probability of phase formation. Therefore, it is important to understand the thermodynamic driving forces in the system to be able to come to an expression for ΔG_ϕ^*.

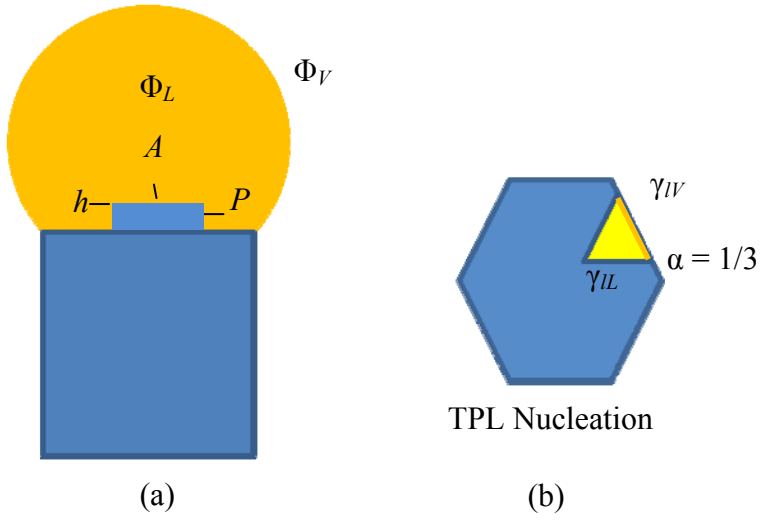

Figure 4.1: Illustration of the nucleation process (a) at the liquid-solid interface. (b) showing.

In this system, the growth species arrive to the Au droplet from the highly supersaturated adatom phase, with chemical potential $\Delta\mu_{AS} = k_B T \ln(\Phi_A)$, where Φ_A is the supersaturation ratio of the adatoms on the surface. The adatoms alloy with the Au droplet to form a supersaturated liquid alloy with chemical potential $\Delta\mu_{LS} = k_B T \ln(\Phi_L)$, where Φ_L is the supersaturation ratio of the growth species in the Au droplet. The nucleation takes place at the TPL, and the Gibbs-free energy of formation is given by:

$$\Delta G_j = -(\frac{A_j.h_j}{\Omega_j})\Delta\mu_{LS,j} + (P_j.h_j)\Gamma_{l,j} + A_j\psi_j, \qquad (4.3)$$

where the subscript j refers to either InP or GaP, h_j is the height of the nucleus which is equivalent to one monolayer, A_j is the area of the nucleus = ar_j^2 and P_j is the lateral perimeter of the nucleus = pr_j. These parameters are illustrated in Figure 4.1. The

parameter ψ_j represents the difference in cohesive energy between the ZB and the WZ phase, given that $\psi_j\big|_{ZB} = 0$. The nucleus surface energy is given by:

$$\Gamma_l = \left[(1-\alpha)\gamma_{lL} + \alpha\gamma_{lV}\right] \tag{4.4}$$

where α is the portion of the nucleus exposed to the vapor phase at the TPL, γ_{lL} is the surface energy between the solid-liquid interface and γ_{lV} is the lateral surface energy of the nucleus with the vapor phase which depends on the phase of the formed nucleus and it take the values of $\gamma_{lV} = \gamma_{ZB}, \gamma_{WZ}$ for ZB and WZ, respectively. The factor f is defined as $f = \gamma_{WZ}/\gamma_{ZB}$ and is less than unity [9]-[11]. The radius of the critical nucleus and the expression for the nucleation barrier are derived by differentiating Eq. (4.3) and equating it to zero. The outcome is an expression for the radius of the formed nucleus,

$$r_j^* = \frac{p}{2A}\frac{\Omega_j \cdot \Gamma_{j,\phi}}{\left(\Delta\mu_{LS,j} - \Omega_j\psi_\phi/h\right)}. \tag{4.5}$$

By Substituting Eq. (4.5) into Eq. (4.3), we obtain

$$\Delta G_{j,\phi}^* = \frac{p^2}{4A}\frac{\Omega_j h \cdot \Gamma_{j,\phi}^2}{\left(\Delta\mu_{LS,j} - \Omega_j\psi_\phi/h\right)}. \tag{4.6}$$

The value of ΔG_ϕ^* varies from WZ and ZB as well as from InP and GaP. In the following section, we will discuss the results obtained from our samples and their interpretations. The above model will also be applied to our case to provide further insight on the phase change in our samples.

4.2 Results and Discussion

Four NW samples were fabricated. The growth temperature for all samples was 430°C. The flux of the growth species was varied among these samples. The net amount of atoms contributing to the growth was similar in all samples. This was achieved by adjusting the growth duration. For sample A, the group-III flux was 2 μm/h for a duration of 10 minutes. Samples B and C were grown with a group-III flux of 1 μm/h and 0.25 μm/h, respectively, for durations of 20 minutes and 80 minutes, respectively. For the first three samples, the V/III flux ratio was set at 1.75. For sample D, the growth rate was 0.25 μm/h and the V/III flux ratio was raised to 8, for a duration of 80 minutes. Table 4.1 summarizes the growth conditions for all our samples.

The NWs from the four samples were sonicated on a TEM grid. The Au-seed diameter distribution of the sonicated NWs that we characterized ranged from 4 nm to 40 nm. The resultant crystal phase of these NWs varied among the four samples. For comparisons between the NWs from the four samples, we have considered the crystal structure at the bottom of 100 nm segment of each NW. In addition, when the model is compared to the experimental results that contain a variety of NW heights, it is simpler to compare the model equations at the bottom of the NWs with the results, rather than choosing other random points along the NW height.

The TEM images and selected area diffraction patterns of the NWs, aligned on the $<\bar{2}\ 1\ 1\ 0>$ zone axis, revealed that NWs were primarily WZ. As the NW diameter increased within the same sample, more ZB insertions occurred and the ZB segment length increased. Figure 4.2 (a) shows a NW with a seed diameter of 4nm, with pure fault-free WZ phase at the bottom of the NW. On the other hand, Figure 4.2 (b) shows a NW with a larger Au seed diameter of 16 nm and ZB insertions within the WZ crystal appears at the bottom of the NW.

Table 4.1 Growth conditions for the samples.

Sample	Temperature T (°C)	Group-III growth rate (μm/h)	V/III flux ratio
A	430	2	1.75
B	430	1	1.75
C	430	0.25	1.75
D	430	0.25	8

Among the samples, sample A showed longer segments of the ZB phase when compared to a NW with similar Au-seed diameter from sample B, as shown in Figure 4.3. The NWs in samples C had much longer segments of pure WZ phase with the majority having one stacking fault within the bottom 100 nms and many were fault-free. Sample D acquired the least stacking fault density, having NWs that are pure WZ phase and fault-free.

Based on the above findings, a preliminary conclusions can be assumed which would states that the ZB insertions in the NWs increased as the growth rate increased. Ultimately, the increase in growth rate translates to a growth with higher supersaturation of the growth species, and it leads to higher probability of ZB formation. This conclusion can be true in the case of single element group-IV growths or binary III-V compounds, where the NW elemental composition is homogenous and does not vary with growth rate. In these cases, the higher growth rate can be translated to a higher supersaturation of the growth species, because other factors that can affect the crystal structure can be pinned as

constants. For example, if the growth rate is the variable among the samples, then the temperature and the NW composition is the same and do not vary.

In our case of InGaP NW growth, if the growth rate is varied, other variables, such as temperature, can be pinned as constants. However, a change in the composition along the NW length and radius is observed as the growth rate is varied [14]. This change in elemental composition can play a role in the change in crystal structure of the NW, simultaneously with the variation in the growth rate. Therefore, the assumption of increased ZB insertions due to higher growth rate or higher supersaturation cannot standalone for the effect of the composition crystal structure has to be simultaneously considered. As a result, we have to separate species that can nucleate, and separately calculate the probability of phase formation taking into account the composition of the NW.

It was also shown [14] that composition of the NW changes with growth rate and diameter. Among the samples, the In concentration in the NWs increased as the growth rate increased and for NWs of the same sample, the In fraction decreased as the NW seed diameter shrunk. By comparing the In behaviour and the stacking fault behaviour, we can then conclude that the change in the In fraction in the NWs is the main cause for ZB formation and the link between the dependence of the crystal structure on the growth rate. In other words, the In is the promoter of the ZB phase in the NWs and as its fraction increase, the ZB formation in the NW increase.

Now, is the In the only promoter of the ZB phase formation? For NWs that grew In-free like the ones in sample C [14], does the pure GaP NW promote ZB or WZ? We conclude that GaP growth promotes the WZ crystal structure only. This is attributed to our results, where NWs with very small diameters in sample A and B with very small In fraction tend to have long periods of pure WZ phase, as shown in Figure 4.2 (a). In addition, for wider range of diameters in sample C, the NWs had small traces of In and they were mostly WZ.

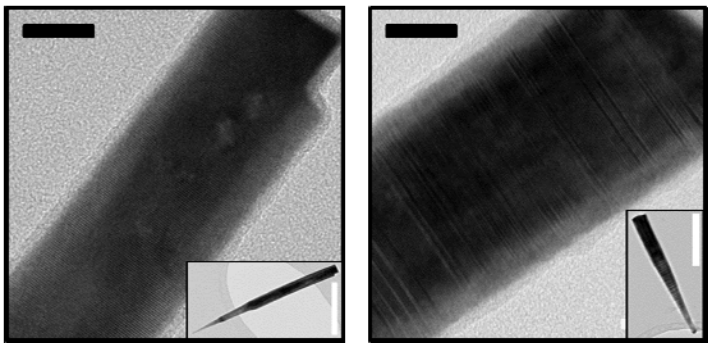

(a) (b)

Figure 4.2 TEM image of two nanowires from the same sample B. (a) NW with Au seed diameter of 4 nm with puze WZ phase and (b) NW with Au seed diameter of 16 nm showing a WZ phase with ZB insertions. Bar is 20 nm

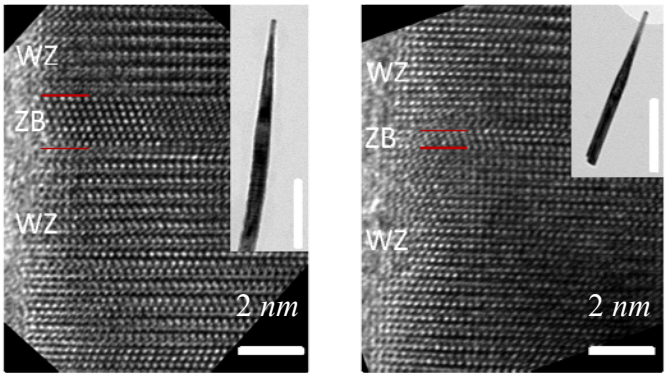

(a) (b)

Figure 4.3 HR-TEM images showing the typical difference between the length of ZB insertions for NWs of similar radii from sample (a) A and (b) B.

To further justify this conclusion, a unique NW within sample C illustrates the effect of In on the change in the crystal structure. The NW shown in Figure 4.4, has its bottom portion of pure WZ phase that is completely fault-free. At the onset line shown in Figure 4.4, mixed phases started to appear. Energy dispersive x-ray (EDX) analysis on the point just before the onset of faults showed that the In composition was x_{In}=0.09. Just beyond the onset line the composition jumps to x_{In}=0.5. This shows that the crystal structure is strongly dependent on In fraction within the NWs in support of our conclusion above. NWs grown to be In-free due to small seed diameter or low growth rate are mainly WZ in phase, and thus, GaP promotes the WZ phase. This translate to setting $P_{WZ,GaP}$ in our model to be equal to unity in all our samples.

In order to find the overall probability of phase formation in the NWs, the kinetic model should be solved to find $\bar{F}_{In}$ and $\bar{F}_{Ga}$, and the nucleation-based model solved for the nucleation barriers for each crystal phase. The kinetic model has been separately discussed in Chapter 3. In addition, we assumed that the probability of WZ formation for GaP is always set to unity for all our samples. The remaining part is solving the nucleation-based model for InP.

In this section, our goal is to calculate $\Delta G^{*}_{\phi,InP}$ for the four samples and its Au-seed diameter dependence, using the variables $\Delta\mu_{LS}$, γ_{lL}, γ_{lV}, f and ψ. The difference between the cohesive energies of ZB and WZ phase ψ was tabulated by Dubrovskii et. al [11] for several semiconductors. We take the value $\psi_{InP} = 6.8\ meV$ and $\psi_{GaP} = 18.3\ meV$ [6][10][12]. In the case of γ_{lV}, values in literature varied significantly. Values calculated using the expression for Kossel crystal [10] showed $\gamma_{lV} = 0.125\ J/m^2$ compared to $\gamma_{lV} = 2\ J/m^2$ for GaP [11]. Another example is InAs, where values were $\gamma_{lV} = 0.57\ J/m^2$ [6] compared to $\gamma_{lV} = 1\ J/m^2$. For InP, reference [11] gives

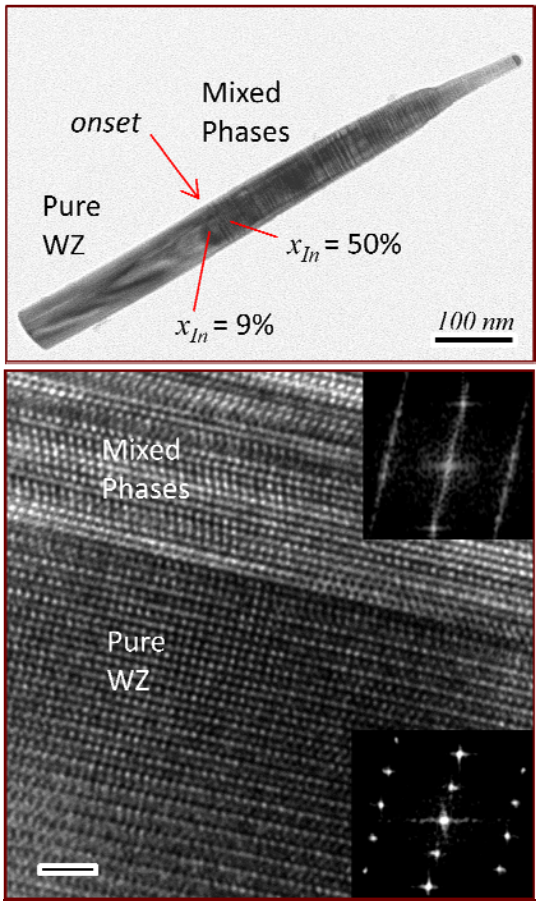

Figure 4.4 NW from sample C (a) showing the onset of mixed phase formation. (b) HR-TEM image at the onset line, showing the pre-onset pure WZ phase and the mixed phases formed after onset.

$\gamma_{lV} = 1.3\ J/m^2$ compared to $\gamma_{lV} = 1\ J/m^2$. For InP, reference [11] gives $\gamma_{lV} = 1.3\ J/m^2$. Generally, the value of γ_{lV} varied significantly in the literature over an order of magnitude. Therefore, we took the value of γ_{lV} to be a fitting parameter and we found that $\gamma_{lV,InP} = 0.6\ J/m^2$ and $\gamma_{lV,GaP} = 1\ J/m^2$ fit our results.

The factor f in the literature has often been taken as a fitting parameter. Its value has been roughly estimated to be around 0.66 when comparing the average lateral surface energies of ZnS nanoparticles in ZB and WZ phase [10]. Practically, the values of f should be between 0.5 and unity, and in our simulations, we found that the value $f = 0.86$ for the InP and GaP.

Our simulations showed that the GaP has a probability equal to unity as discussed above. Therefore, through the rest of our discussion, we will only deal with the InP portion in the equations of the model, to find the probability of crystal phase formation within the NWs.

Au Size effect

There are three parameters in our model that contribute to the Au size influence on the crystal structure. They are $\bar{F}_{In}$, $\Delta\mu_{LS}$ and γ_{lL}. Firstly, the flux factor $\bar{F}_{In}$ decreases with the decrease in the Au seed diameter, as analysis in Chapter 3 showed. However, during our simulations and optimization processes, this effect could not have been solely responsible for the decrease in the fault formation and hence, other contributors had to be included. Secondly, there is not an exact formula that estimates for the exact value of the chemical potential $\Delta\mu_{LS}$. The only criteria known for the chemical potential of a species

in the liquid alloy is $\Delta\mu_{AS} > \Delta\mu_{LS} > \Delta G^*$ to ensure the thermodynamic picture for NW growth. Therefore, we used the upper limit of $\Delta\mu_{LS}$ as its value and set $\Delta\mu_{LS} = \Delta\mu_{AS}$. The value of $\Delta\mu_{AS}$ can also be derived from the growth model in Chapter 3, and it has a dependence on the diameter of the Au droplet. However, combining $\bar{F}_{In}$ and in the model was not enough to fully captures the Au shrinking effect.

Investigations done in the previous Chapter reported the shrinkage of the Au seed particle during the cool down period. Very small particles shrunk more than larger seed particles and it was found that small Au particles are nearly free from any In or Ga as they were all purged out during the cool down period that follow the growth [14]. The original volume of the Au droplet was estimated from the diameter of the NW's tip before the cool down region, and all the excess volume was estimated to be from In and Ga. The overall surface tension of the Au alloy particle γ_{LS} was calculated and was found to be dependent on the Au seed diameter[15]. The value of γ_{LS} ranged from 1 to 1.2 J/m^2 for particle with large diameters and decreased as the diameter decreased. The decrease with the diameter is because the percentage of In and Ga in the droplet compared to Au is higher during growth. Provided that In and Ga have lower surface tensions than Au, as their percentage increase, the overall surface tension of the droplet decrease.

Although γ_{LS} does not directly appear in our equations for the nucleation-based model, there exist a boundary at the TPL shared by γ_{LS}, γ_{lV} and γ_{lL}. The Au liquid droplet with it γ_{LS} creates specific contact angles with the lateral surfaces of the nucleus with γ_{lV} on the lateral nucleus-vapor side and γ_{lL} on the lateral nucleus-liquid side. Since we have γ_{lV} as a surface energy that is independent of the Au size effect and γ_{LS} is dependent on the Au diameter size, therefore, it is concluded that γ_{lL} must be dependent on the Au seed diameter size.

To model the Au size dependence of γ_{lL}, we found that the relation $\gamma_{lL}(R) = \gamma_1 - \gamma_2/R$ satisfies our model. The values of γ_1 and γ_2 are used as fitting parameters and were found to be $\gamma_1 = 1.2\ J/m^2$ and $\gamma_2 = 1.2\ J/nm^2$ with radius of the seed droplet *R* is in *nms*.

The probability of WZ formation $P_{WZ,InP}$ is plotted versus the supersaturation ratio of the liquid Φ_L, in Figure 4.5. The figure shows the effect of having a variable γ_{lL} for our model and points out the operating regions of our samples. The effect of γ_{lL} can be understood if we consider the point R_1 in our plot. This point on the green curve resembles a NW with large diameter and $\gamma_{lL} = 1.1 J/m^2$ for a sample with a specific supersaturation ratio. Since the supersaturation ratio in a single sample does not vary significantly with diameter shrinkage, it is assumed in this discussion that it stays constant. As we go on decreasing the NW diameter, the radius R_1 decreases to R_2, and consequently the diameter dependent γ_{lL} decreases from $1.1 J/m^2$ to $0.8 J/m^2$. The NW with the smaller radius R_2 would have a smaller $\gamma_{lL} = 0.8 J/m^2$ and its probability of WZ formation becomes higher than the NW with radius R_1. Similarly, if the NW`s diameter decreases further to the point R_3, with $\gamma_{lL} = 0.5 J/m^2$, the probability of WZ formation becomes higher. This scenario takes place as the NW diameter decreases in each sample, and thus, shifts from low probability of WZ formation for NWs with large diameters and the probability increases as the diameter decreases.

Based on the values of the supersaturation ratio, we found that samples A and B are located on the transition area of the probability curve for InP WZ formation. For sample C, its probability of InP nucleating in the WZ form in nearly zero. Mostly, the NWs in sample C has very limited In which results in WZ GaP NWs, however, as shown in Figure 4.4, as InP starts contributing to growth, the ZB formation becomes as dominant as the WZ from the GaP.

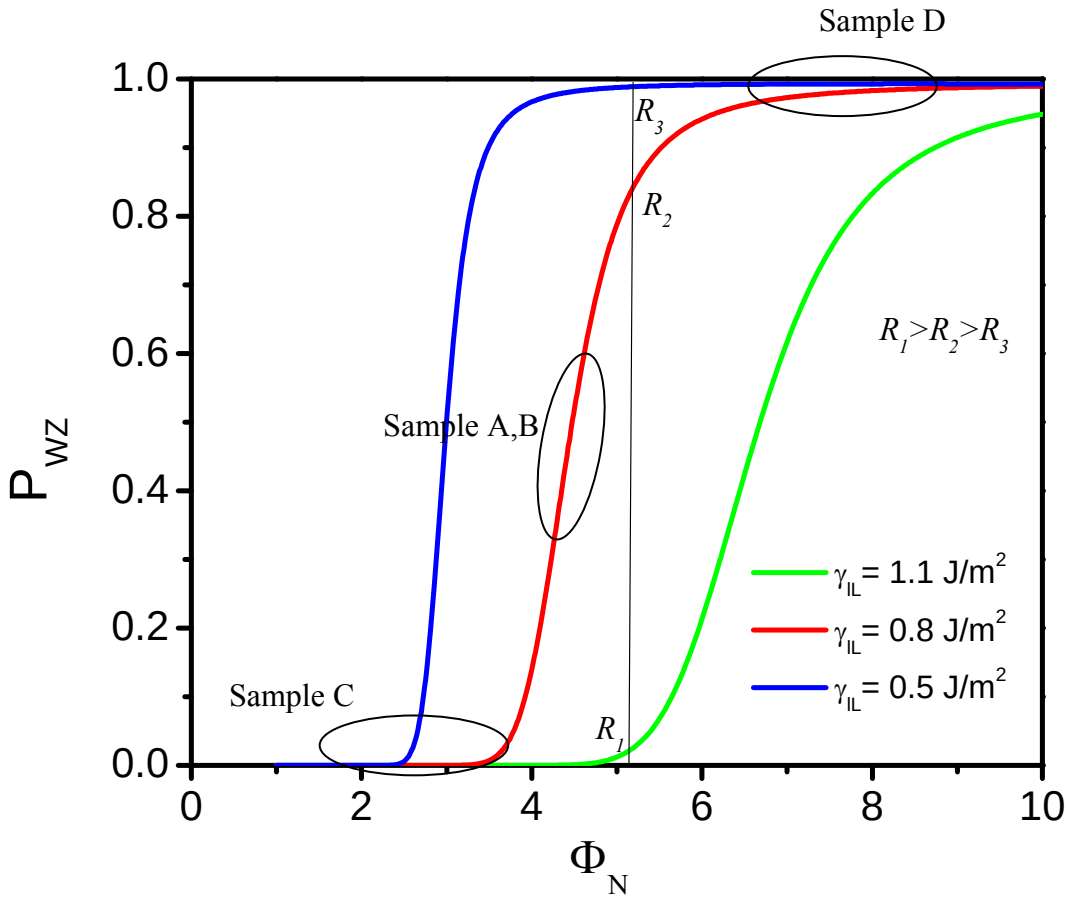

Figure 4.5 The probability $P_{WZ,InP}$ plotted versus the super-saturation Φ_N. Three curves are plotted for different values of γ_{lL}.

The group-V flux is significantly increased in sample D. As a result, its chemical potential for InP formation for the arriving adatoms $\Delta\mu_{AS,InP} = k_B T \ln(\Phi_{A,In}\Phi_{A,P_2}^{1/2})$ increases. This increase in the chemical potential locates sample D at the top of the probability curve, due to its high supersaturation ratio.

In samples C and D, the occurrence of ZB insertions within the NW is low. For samples A and B, due to the abundance of NWs with many ZB insertions within it crystal structure, it was simpler to quantify the amount of ZB segments compared to WZ. The ratio of total length of the measured WZ segments to the total length of the segment (100 *nm*) is taken equivalent to P_{WZ}. The measured results were plotted and compared to our model in Figure 4.6. The model showed the expected behaviour compared to the experimental results. The model did not capture the sample point from sample B that is reaching the unity probability. This value is attributed to the factor $\bar{F}_{In}$ that can reach zero for NWs with very small diameters. This is caused by the randomness of the Au distribution on the surface, where we can find values of $\bar{F}_{In}$ that varies from the average used in the model.

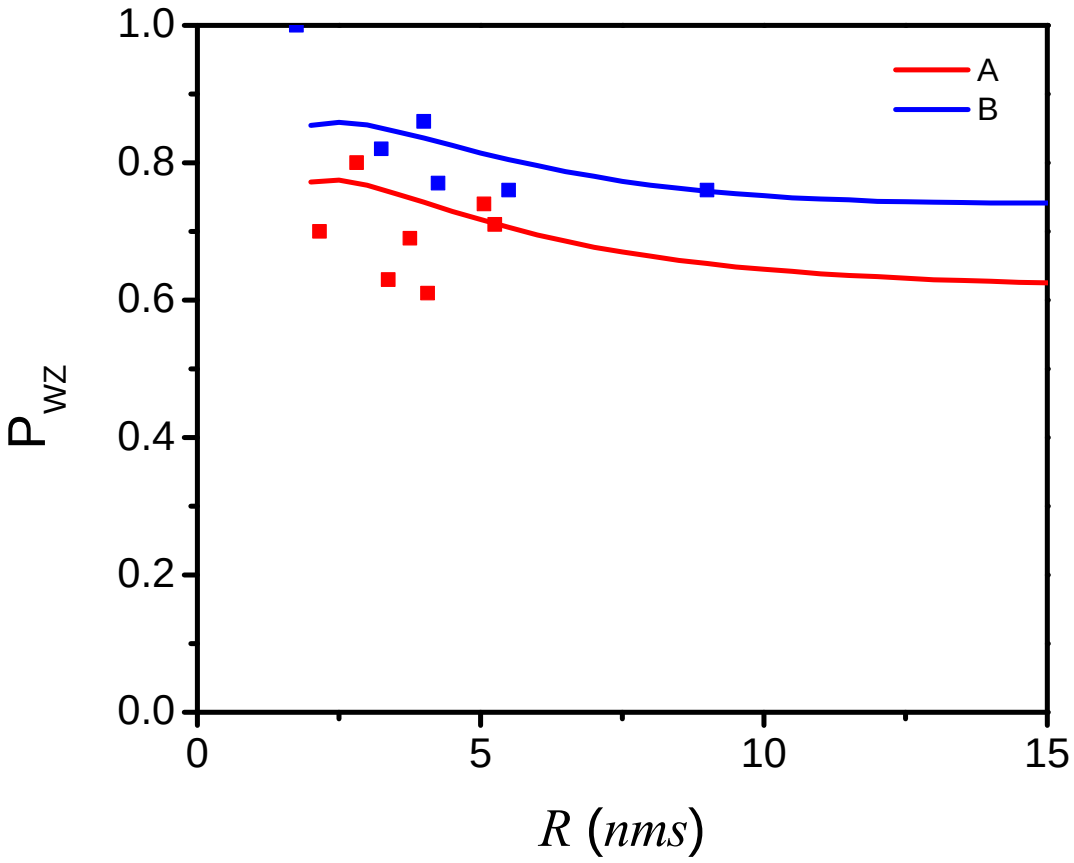

Figure 4.6 Experimental results (dotted data point) for the total length of WZ segments in the bottom 100 *nm* of the NWs from samples A and B and the calculated probability of WZ at the bottom of the NWs (solid lines).

4.3 Conclusion

In this article, we have addressed the change in crystal structure of InGaP due to varying growth conditions. The key to our approach was to assume the nucleation of two separate systems, one for InP and another for GaP. The results showed that the GaP nucleation favors WZ phase formation for all our samples. The ZB phase formation was dependent on the presence of In in the NW, which its concentration depended on the growth conditions and NWs. In-free NWs had WZ crystalline phase.

Utilizing a growth model was important to acquire important parameters that are used as inputs for the nucleation model, such as $\bar{F}_{In}$, $\bar{F}_{Ga}$, Φ_A and γ_{LS}. Another key to our approach is looking at γ_{LS} as a variable and a diameter dependent and its effect on γ_{lL}. We have used $\gamma_{lL}(R)$ as a fitting function to model the diameter dependence of the phase formation. Probability plots were used to explaining the effect of $\gamma_{lL}(R)$ on our samples. In addition, we pointed out the operating regions for the four samples. Finally, we were able to fit the our experimental results to our simulations.

References

[1] J. A. Czaban, D. A. Thompson, and R. R. LaPierre, Nano Letters 9, 148 (2009).

[2] F. Patolsky, G. Zheng, C. Lieber, Anal. Chem. 78 (13) (2006).

[3] C. P. T. Svensson, M. Thomas, T. Johanna, L. Christina, R. Michael, H. Dan, S. Lars, and O. Jonas, Nanotechnology, 305201 (2008).

[4] X. Jiang, Q. Xiong, S. Nam, F. Qian, Y. Li, and C. M. Lieber, Nano Lett. 7, 3214 (2007).

[5] K. A. Dick, P. Caroff, J. Bolinsson, M. E. Messing, J. Johansson, K. Deppert, L. R. Wallenberg, and L. Samuelson, Semicond. Sci. Technol. 25 (2010).

[6] H. J. Joyce, J. Wong-Leung, Q. Gao, H. H. Tan, and C. Jagadish, Nano Letters 10, 908 (2010).

[7] T. Akiyama, K. Nakamura, and T. Ito, Physical Review B (Condensed Matter and Materials Physics) 73, 235308(2006).

[8] T. Akiyama, K. Sano, K. Nakamura, and T. Ito, Japanese Journal of Applied Physics 45, L275 (2006).

[9] F. Glas, J. C. Harmand, and G. Patriarche, Physical Review Letters 99, 146101 (2007).

[10] J. Johansson, L. S. Karlsson, K. A. Dick, J. Bolinsson, B. A. Wacaser, K. Deppert, and L. Samuelson, Crystal Growth & Design 9, 766 (2009).

[11] V. G. Dubrovskii and N. V. Sibirev, nical Physics Letters 35, 380 (2009).

[12] J. Johansson, K. A. Dick, P. Caroff, M. E. Messing, J. Bolinsson, K. Deppert, and L. Samuelson, The Journal of Physical Chemistry C 114, 3837 (2010).

[13] J. Johansson, J. Bolinsson, M. Ek, P. Caroff, and K. A. Dick, ACS Nano 6, 6142 (2012)

[14] A. Fakhr and et al., Nanotechnology 21, 165601 (2010).

[15] Modelling of InGaP Nanowire Morphology, Composition and Structure on Molecular Beam Epitaxy Growth Conditions

Chapter 5

5.1 Summary and Conclusion

Throughout our discussion in the chapters of this thesis, we have been dealing with the growth of ternary InGaP nanowires. These types of nanowires do not have a recipe of growth similar to that of a thin film two-dimensional epitaxial growth. The composition of the nanowires had an unpredictable behaviour at high temperatures, where the nanowires appeared In-free and their density on the surface was very low. Lowering the growth temperature to 430 ºC, favored the In, where we were able to detect it in our samples, and the density of the nanowires was much higher compared to the high temperature growth.

Further analysis on the nanowires indicated that the grown nanowires have a non-homogenous concentrations of In and Ga. Elemental distribution analysis showed that the nanowires form a core/shell structure, where the core is In-rich and the shell is Ga-rich. These results were supported by EDX radial line scans and similar line scans performed on microtomed disks of the nanowires along with HAADF imaging. The model described in chapter 3 attributed the formation of this structure, to the higher diffusion length of In on the nanowire facets that would allow it to reach the Au droplet at a higher rate compared to Ga. Meanwhile, due to its lower diffusion length on the nanowire sidewalls, Ga nucleated as GaP on the sidewalls, promoting radial growth and forming the shell. In addition, the simulations of the model in chapter 3, with In having higher diffusion length

on the sidewall, revealed the reason for having and increasing In fraction along the nanowire axis.

The key approach in modelling such a ternary system, was to break the analysis into the simplest form. We took advantage of the fact that when ternary systems are grown, such as InGaP, the nucleation takes place in the form of InP and GaP separately. Therefore, we derived model equations for each of the growth species separately to see the impact of the growth conditions on each one by its own.

Starting from the vapor phase, the GaP had much higher supersaturation than InP, for both of its growth species (Ga and P_2(GaP) versus In and P_2 for(InP)). This allowed the GaP to be more resilient to growth conditions and contribute to the nanowire all the time. Meanwhile, the InP with its low supersaturation was sensitive to variations in temperature, growth rate and Au particle distribution on the surface. Consequently, the model was able to describe the In deficiency that takes place at high temperature, low growth flux which does not create enough driving force of the InP and finally, for small Au diameters due to the low surface diffusion length.

Changes in the crystal structure of the nanowires was also attributed to the difference in the nucleation of InP versus GaP. Similar to the growth model, we dealt with the InP and the GaP separately and derived an expression that combines the kinetic growth model of the system along with the thermodynamic nucleation-based model. It was found that nanowires with limited or no presence of In (pure GaP) had WZ crystal structure. Therefore, it was concluded that GaP favors WZ crystal formation for all the growth conditions of our samples. As a result, our focus was totally on the analysis of the crystal phase formation of the InP, as it was responsible for the crystal phase change. The model described the regions of operations of our samples with respect to the probability of WZ formation of In. Finally, we focused on the Au droplet's size effect and attributed the decrease in ZB formation of InP for small diameters to the change in the surface energy of the droplet.

5.2 Future Work

The vision at the start of this work was to grow ternary and quaternary semiconductor NWs. As challenges arise, a comprehensive understanding of the ternary NW growth was necessary. The growth model along with the nucleation-based model, developed in Chapters 3 and 4, assisted in understanding the physical phenomena that takes place during ternary growths. However, additional experiments are needed to concluded the recipe for the growth of ternary InGaP NWs with the desired crystal structure and elemental distribution.

The growth model, discussed in Chapter 3, was based on the assumption that impingement on the NW sidewalls was neglected. The model showed a great fit to our experimental data, however, for a more general case, the NW sidewall impingement should be taken into account. In addition, the model should be extended to explain other combination of ternary and quaternary compounds.

The grown NWs showed few interesting features, such as having a core/shell structure and an incremental elemental composition along the NW's length. While core/shell structures in NWs has been investigated, it would be of great interest to examine the effect of the incremental elemental distribution using photoluminescence (PL) measurements. Another area of interest is to explore utilizing these NWs as device and take advantage from their incremental composition change.